

# nuSTORM and a Path to a Muon Collider

David Adey,<sup>1</sup> Ryan Bayes,<sup>2</sup> Alan D. Bross,<sup>1</sup>  
and Pavel Snopok<sup>3</sup>

<sup>1</sup>Accelerator Physics Center, Fermi National Accelerator Laboratory, Batavia, Illinois 60510

<sup>2</sup>School of Physics and Astronomy, University of Glasgow, Glasgow G12 8QQ,  
United Kingdom

<sup>3</sup>Department of Physics, Illinois Institute of Technology, Chicago, Illinois 60616

Annu. Rev. Nucl. Part. Sci. 2015. 65:145–75

First published online as a Review in Advance on  
May 20, 2015

The *Annual Review of Nuclear and Particle Science*  
is online at [nucl.annualreviews.org](http://nucl.annualreviews.org)

This article's doi:  
10.1146/annurev-nucl-102014-021930

Copyright © 2015 by Annual Reviews.  
All rights reserved

## Keywords

sterile neutrinos, neutrino cross sections, ionization cooling, muon collider

## Abstract

This article reviews the current status of the nuSTORM facility and shows how it can be utilized to perform the next step on the path toward the realization of a  $\mu^+\mu^-$  collider. This review includes the physics motivation behind nuSTORM, a detailed description of the facility and the neutrino beams it can produce, and a summary of the short-baseline neutrino oscillation physics program that can be carried out at the facility. The basic idea for nuSTORM (the production of neutrino beams from the decay of muons in a racetrack-like decay ring) was discussed in the literature more than 30 years ago in the context of searching for noninteracting (sterile) neutrinos. However, only in the past 5 years has the concept been fully developed, motivated in large part by the facility's unmatched reach in addressing the evolving data on oscillations involving sterile neutrinos. Finally, this article reviews the basics of the  $\mu^+\mu^-$  collider concept and describes how nuSTORM provides a platform to test advanced concepts for six-dimensional muon ionization cooling.

## Contents

|   |     |
|---|-----|
| 1. OVERVIEW .....   | 146 |
| 2. nuSTORM'S PHYSICS PROGRAM: THREE THEMES .....  | 147 |
| 2.1. Sterile Neutrinos .....  | 148 |
| 2.2. Neutrino Scattering Physics: Systematics of Long-Baseline<br>Neutrino Oscillation Measurements ..... | 149 |
| 3. THE nuSTORM FACILITY .....   | 151 |
| 3.1. Decay Ring .....   | 154 |
| 3.2. Low-Energy Muon Beam .....   | 154 |
| 3.3. Beam Instrumentation .....   | 155 |
| 4. DETECTOR DESIGN FOR THE nuSTORM NEUTRINO<br>PHYSICS PROGRAMS .....                                     | 156 |
| 5. PERFORMANCE OF THE nuSTORM FACILITY: NEUTRINO PHYSICS ...  | 157 |
| 5.1. Neutrino Beams Produced at nuSTORM .....   | 158 |
| 5.2. nuSTORM's Sensitivity to Sterile Neutrinos .....   | 160 |
| 6. PATH TO A MUON COLLIDER .....  | 166 |
| 6.1. Introduction .....   | 166 |
| 6.2. Ionization Cooling Overview .....  | 166 |
| 6.3. Six-Dimensional Cooling Channels .....   | 168 |
| 6.4. Six-Dimensional Cooling Tests .....  | 170 |
| 7. MUON ACCELERATOR STAGING STUDY: RATIONALE FOR A STAGED<br>APPROACH .....                               | 170 |
| 8. SUMMARY AND OUTLOOK .....  | 171 |

## 1. OVERVIEW

The nuSTORM facility (1–3) is the simplest implementation of the neutrino factory concept (4) and is based almost entirely on well-demonstrated accelerator technology, thus making its implementation technically feasible as of early 2015. At the heart of the facility is a racetrack-like muon storage ring that can deliver beams of  $\bar{\nu}_e$  and  $\bar{\nu}_\mu$  from the decay of stored  $\mu^\pm$  beams. At nuSTORM, searches can be carried out to look for the existence of sterile neutrinos, and simultaneously a physics program can operate that serves future long-baseline (LBL) and short-baseline (SBL) neutrino oscillation programs by providing definitive (percent-level precision) measurements of  $\bar{\nu}_e N$  and  $\bar{\nu}_\mu N$  scattering cross sections over a wide (0.5 to  $\simeq 4$  GeV) neutrino energy range. The facility also provides a platform to develop and test concepts for six-dimensional (6D) muon cooling and thus facilitates the research and development (R&D) path for a muon collider.

The front end of nuSTORM is essentially identical to a conventional neutrino beam in which protons (80–120 GeV) are used to produce pions off a conventional solid target and the pions are then focused with a magnetic horn (5; see the sidebar). From there, nuSTORM departs significantly from a conventional neutrino beam. After the horn, quadrupole magnets are used to transport the pions to a chicane (a double bend for sign selection), and then either a  $\pi^-$  or  $\pi^+$  beam is transported to, and injected into, the decay ring. The pions that decay in the first straight section of the ring can yield muons that are captured in the ring. (Note that the pion decays also

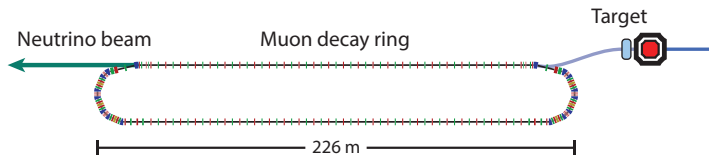


**Figure 1**

Schematic layout of the nuSTORM facility.

## NEUTRINO BEAMS

It has been more than 50 years since Simon van der Meer invented the magnetic horn in order to improve the performance of neutrino beam production. The nuSTORM facility provides a technically ready opportunity to finally move beyond this paradigm.

produce a very powerful  $\nu_\mu$  beam; see Section 5.1.) The circulating muons then subsequently decay into electrons and neutrinos.

The nuSTORM facility uses a storage ring design that was optimized for a 3.8 GeV/ $c$  muon central momentum. This momentum was selected to maximize the physics reach for both neutrino oscillation and neutrino cross-section physics (see **Figure 1** for a schematic of the facility).

The physics potential of nuSTORM, as in the case of the neutrino factory (6), comes from the fact that muon decay yields a neutrino beam of precisely known flavor content and energy (the muon energy is defined by the ring lattice). If the circulating muon flux in the ring is measured accurately [with beam-current transformers (BCTs), for example], then the neutrino beam flux can be determined to high precision ( $\lesssim 1\%$ ). This level of precision can be obtained without the need for any input or assumptions regarding particle production rates, proton targeting stability, target structural stability, or horn pulse-to-pulse uniformity, the understanding of which is of tremendous importance for a conventional neutrino beam.

## 2. nuSTORM'S PHYSICS PROGRAM: THREE THEMES

The physics program for the nuSTORM facility encompasses three central themes.

1. The neutrino beams produced at the nuSTORM facility will enable SBL oscillation searches for light sterile neutrinos with unprecedented sensitivity over a wide parameter space and, if sterile neutrinos are discovered, will offer the opportunity to carry out an extremely comprehensive study of their properties.
2. These same beams may be exploited to make detailed studies of neutrino–nucleus scattering over the neutrino energy range of interest to present and future LBL neutrino oscillation experiments, such as T2HK (7), LBNE (8), and LBNO (9).
3. The storage ring itself, and the muon beam it contains, can be used to carry out an R&D program that can facilitate the implementation of the next step in the incremental development of muon accelerators for particle physics.

These three individually compelling themes provide the scientific and technological case for nuSTORM.

## 2.1. Sterile Neutrinos

Sterile neutrinos are a generic ingredient of many extensions of the Standard Model and, even in models that do not contain them, can usually be easily added. An important class of sterile neutrino theories comprises models explaining the smallness of neutrino masses by means of a seesaw mechanism. In its simplest form, the seesaw mechanism requires at least two heavy ( $\sim 10^{14}$  GeV) sterile neutrinos that would have very small mixings ( $\sim 10^{-12}$ ) with the active neutrinos. However, in slightly nonminimal models, at least one sterile neutrino can have a much smaller mass and a much larger mixing angle. Examples of this type of model include the inverse seesaw (10, 11) and the split seesaw (12) scenarios. For a detailed review of models with sterile neutrinos and their associated phenomenology, see Reference 13.

**2.1.1. Experimental status for light sterile neutrinos.** Much of the current interest in light sterile neutrinos is motivated by experimental data. Results from the LSND (14) and MiniBooNE (15) experiments, data from the GALLEX and SAGE solar neutrino experiments (16–20), and a reanalysis (21–23) of SBL ( $L \leq 100$  m) reactor experiments can be described by a  $3 + 1$  model with 3 active neutrinos and 1 sterile neutrino with a mass of  $\simeq 1$  eV and small mixing. The appearance signals ( $\nu_\mu \rightarrow \nu_e$  and  $\bar{\nu}_\mu \rightarrow \bar{\nu}_e$ ) observed by LSND and MiniBooNE imply the existence of a corresponding disappearance signal via the following inequality (24):

$$\langle P_{\nu_\mu \rightarrow \nu_e} \rangle \leq 4(1 - \langle P_{\nu_\mu \rightarrow \nu_\mu} \rangle)(1 - \langle P_{\nu_e \rightarrow \nu_e} \rangle), \quad 1.$$

where  $\langle P_{\nu_\mu \rightarrow \nu_e} \rangle$ ,  $\langle P_{\nu_\mu \rightarrow \nu_\mu} \rangle$ , and  $\langle P_{\nu_e \rightarrow \nu_e} \rangle$  are the energy-averaged oscillation probabilities for  $\nu_\mu \rightarrow \nu_e$  appearance and  $\nu_\mu \rightarrow \nu_\mu$ ,  $\nu_e \rightarrow \nu_e$  disappearance, respectively. An analogous expression is valid for antineutrinos. This disappearance signal has been observed in GALLEX and SAGE ( $\nu_e$ ) and in the SBL reactor experiments ( $\bar{\nu}_e$ ).

Despite the interesting results from the experiments described above, the existence of light sterile neutrinos is far from established. Several other SBL experiments (E776, KARMEN, NOMAD, ICARUS) did not observe an appearance signal (25–28), and strong constraints on a disappearance signal have been produced by numerous other experiments (data from LBL and SBL experiments, solar and atmospheric neutrino data, etc.) (17, 19, 29–57). These data place strong constraints on the available sterile neutrino parameter space. The compatibility of the signals from the LSND, MiniBooNE, reactor, and gallium experiments with null results from the large number of other experiments has been assessed in global fits (13, 58–65). **Figure 2** shows the results from one of these studies (65). The parameter region favored by the LSND, MiniBooNE, reactor, and gallium experiments is incompatible, at the 99% CL, with exclusion limits from all other experiments. It is difficult to resolve this tension, even in models with more than one sterile neutrino. Recent results from DAYA BAY, MINOS+, and T2K (66–68) have placed additional constraints on the allowed parameter space but do not significantly alter the conclusions from **Figure 2**. Note that despite the incompatibility between the appearance and disappearance data sets used in the global fit, taken individually, each different data set is self-consistent. For example,  $\bar{\nu}_\mu \rightarrow \bar{\nu}_e$  transitions with parameters suitable for explaining LSND and MiniBooNE are not directly ruled out by other experiments obtaining null results measuring the same oscillation channels (65).

Finally, cosmological observations constrain the effective number ( $N_{\text{eff}}$ ) of neutrinos and the sum of neutrino masses, placing tight constraints on the allowed parameter space for light sterile neutrinos. Recent Planck data (69) yield  $N_{\text{eff}} = 3.30^{+0.54}_{-0.51}$  when combined with polarization data from WMAP (70), high-multipole measurements from ACT (71) and SPT (72, 73), and data on baryon acoustic oscillations (BAO) (74–77). The same data impose a constraint on  $\sum m_\nu \leq 0.230$  eV at the 95% CL. However, cosmology places constraints on sterile neutrinos that are

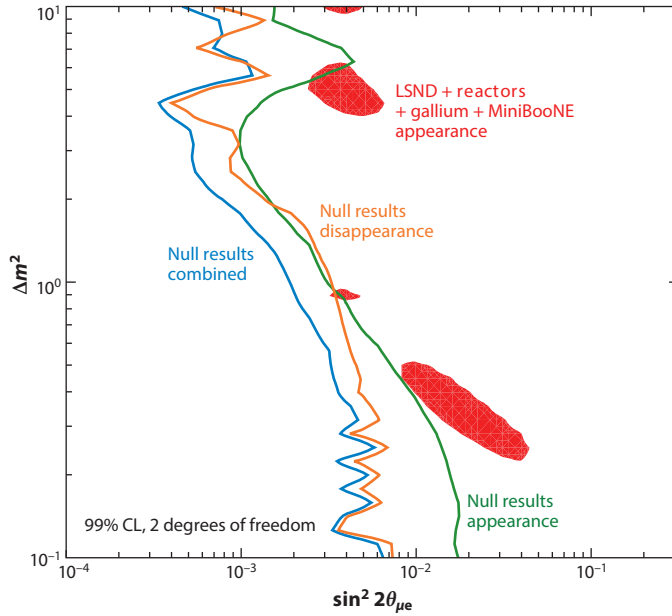


**Figure 2**

Results of a global fit (65) to data in a 3+1 sterile neutrino model. The solid red areas indicate the regions preferred by the experiments reporting a signal (LSND, MiniBooNE, reactors, and gallium) versus the constraints imposed by disappearance null results (*orange*), appearance null results (*green*), and all null results combined (*blue*).

thermalized in the early Universe; models with sterile neutrinos, with so-called hidden interactions (78, 79), reconcile the tension between cosmology and the experimental data indicating a light sterile neutrino. A recent paper (80) has extended this argument, showing that this scenario would reduce  $N_{\text{eff}}$  to 2.7.

We end our discussion on the experimental status of light sterile neutrinos by stating that, given the current situation, it is impossible to draw firm conclusions regarding their existence. An experiment with superior sensitivity and precisely controlled systematic uncertainties would have great potential to clarify the situation by either finding a new type of neutrino oscillation or by producing a strong and robust constraint against any such oscillation.

## 2.2. Neutrino Scattering Physics: Systematics of Long-Baseline Neutrino Oscillation Measurements

The recent measurement of a large value for the mixing angle ( $\theta_{13}$ ) has made the observation of  $CP$  violation in the lepton sector a fundamental (and now reachable) goal of the next generation of LBL neutrino oscillation experiments. Measurement of the  $CP$ -violating phase ( $\delta_{CP}$ ) can be accessed experimentally through two methods: A nonzero phase will lead to a difference between the  $\nu_\mu \rightarrow \nu_e$  and  $\bar{\nu}_\mu \rightarrow \bar{\nu}_e$  appearance probabilities, as well as a variation in the relative amplitude of the second oscillation maximum with respect to the first oscillation maximum in  $\nu_\mu \rightarrow \nu_e$  appearance measurements. Any experiment that is attempting to measure  $CP$  violation using neutrino oscillations must be capable of measuring a small difference between small numbers

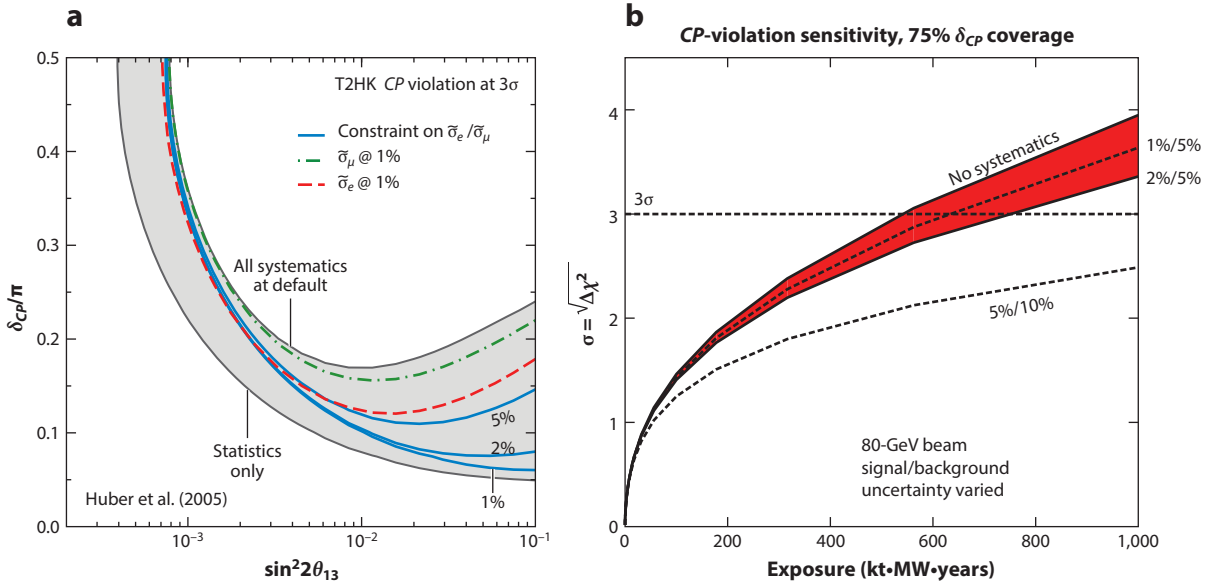


**Figure 3**

(a)  $CP$ -violation sensitivity at  $3\sigma$  for a certain choice of systematic errors and for statistical errors only (curves delimiting the shaded region). Also shown is the sensitivity if certain constraints on the product of cross sections multiplied by efficiencies  $\tilde{\sigma}$  are available: 1% accuracies on  $\tilde{\sigma}_\mu$  and  $\tilde{\sigma}_e$  for neutrinos and antineutrinos and 5%, 2%, and 1% accuracies on the ratios  $\tilde{\sigma}_\mu/\tilde{\sigma}_e$  for neutrinos and antineutrinos. Panel modified from Reference 81. (b) The 75%  $CP$ -violation reach of LBNE at the  $3\sigma$  CL as a function of the total exposure and its change under variations of the systematic error budget on signal normalization and background normalization, respectively.

of events, and in this context, it is imperative that all systematic errors be well controlled by external measurements, measurements at near detectors, or both. One of the largest systematic errors comes from poor knowledge of the neutrino [ $\bar{\nu}_e$  and  $\bar{\nu}_\mu$ ] interaction cross sections, and an irreducible component of this uncertainty is knowledge of the neutrino flux. As discussed in Section 5.1, nuSTORM offers the possibility of reducing the neutrino flux uncertainties by upward of a factor of 10.

A T2HK-like setup has been studied (81) in which more than 20 parameters, including total cross-section uncertainties, were considered. One of the main results is shown in **Figure 3a**, which shows the sensitivity to  $CP$  violation both for statistical errors only and for the full systematic error budget. Clearly, a constraint on the ratio  $\tilde{\sigma}_\mu/\tilde{\sigma}_e$  (where  $\tilde{\sigma}_\mu$  and  $\tilde{\sigma}_e$  are the product of cross section multiplied by detection efficiency for  $\nu_\mu$  and  $\nu_e$ , respectively) is an efficient way to recover the desired statistical sensitivity. Another way to illustrate this problem is shown in **Figure 3b**, which depicts results from an LBNE study (24) in which the capability to measure  $\delta_{CP}$  at  $3\sigma$  sensitivity over 75% of the parameter space is given as a function of exposure for various assumptions regarding the systematic error budget. In order to reach 75% coverage in a reasonable exposure time, systematic uncertainties at the 1% level are necessary. As shown by **Figure 3b**, degradation of the systematic uncertainty to the 5% level corresponds to an exposure increase of roughly 200–300%, which occurs in a very nonlinear fashion.

In order to have the largest  $\delta_{CP}$  coverage, the ratio  $\tilde{\sigma}_\mu/\tilde{\sigma}_e$  needs to be understood at the few-percent level.

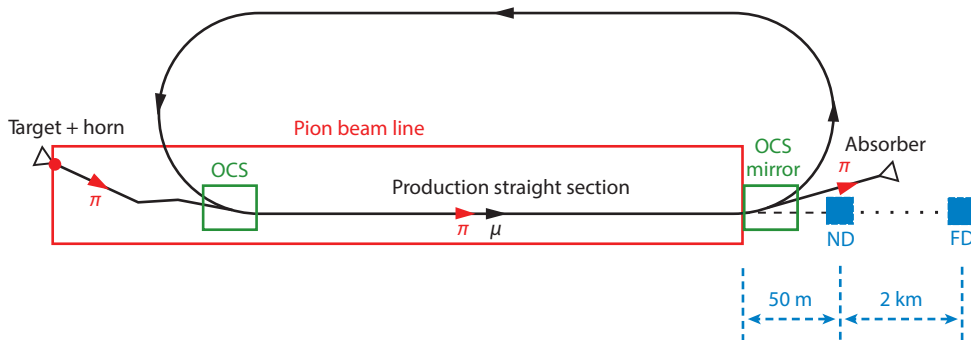


**Figure 4**

Schematic diagram of the nuSTORM facility. The positions of the near detector (ND) and far detector (FD) sites are also shown. The red box shows the components of the facility that constitute what has been termed the nuSTORM pion beam line. Abbreviation: OCS, orbit combination section.

### 3. THE nuSTORM FACILITY

The basic concept for the facility is presented in Section 1, above. After the pions are transported to the decay ring, they are “stochastically” injected into the ring (82, 83), and pion decays within the first straight section of this ring can yield a muon that will be stored in the ring. Muon decay produces neutrino beams of known flux and flavor via  $\mu^+ \rightarrow e^+ + \bar{\nu}_\mu + \nu_e$  or  $\mu^- \rightarrow e^- + \nu_\mu + \bar{\nu}_e$ . nuSTORM uses a storage ring with a central momentum of 3.8 GeV/c ( $\pm 10\%$ ) to obtain a spectrum of neutrinos that peaks at  $\simeq 2$  GeV (see Section 5.1). The pion beam line is optimized to capture and transport pions in a momentum band of  $5 \pm 1$  GeV/c.

The stochastic injection scheme employed by nuSTORM, the feasibility of which was recently confirmed by Liu et al. (84), avoids using a separate pion decay channel and fast kickers, so it requires only dc magnets. **Figure 4** provides a schematic of this concept, illustrating the components of the facility that constitute what has been termed the nuSTORM pion beam line: pion collection downstream of the horn; transport to the ring, which involves a sign-selection chicane; and then injection into the ring via the orbit combination section (OCS) (A. Liu, D.V. Neuffer, A. Bross & S. Lee, manuscript submitted). Pions that do not decay in the first straight section are removed by an OCS mirror and transported to a beam absorber. Muons from forward decay, lying in the same momentum band of the initial pions, are also extracted by the OCS mirror (see Section 3.2).

A complete engineering conceptual design for siting nuSTORM at Fermilab has been completed (85). **Figure 5** shows the nuSTORM facility components as they would be sited at Fermilab. The design of the facility followed, wherever possible (primary proton beam line, target, horn, etc.), NuMI (86) designs and consists of six components: the primary beam line, target station, transport line, muon decay ring, and near and far detector halls. Sited at Fermilab, nuSTORM operation extracts one booster batch ( $\simeq 8 \times 10^{12}$  protons) at 120 GeV from the Main Injector (MI) and places this beam on target. Note that a full store of six booster matches in the MI corresponds to 700 kW of total beam power. The 1.6- $\mu$ s-long booster batch’s length is well matched to the 480-m circumference of the decay ring. Muons captured in the ring will have just returned to the OCS as pion injection stops. A layout concept for siting nuSTORM at CERN has also been developed (87, 88).

The primary proton beam line and target station (and its components, i.e., target and horn) for nuSTORM can closely follow the NuMI designs. A horn optimization study (89) specifically



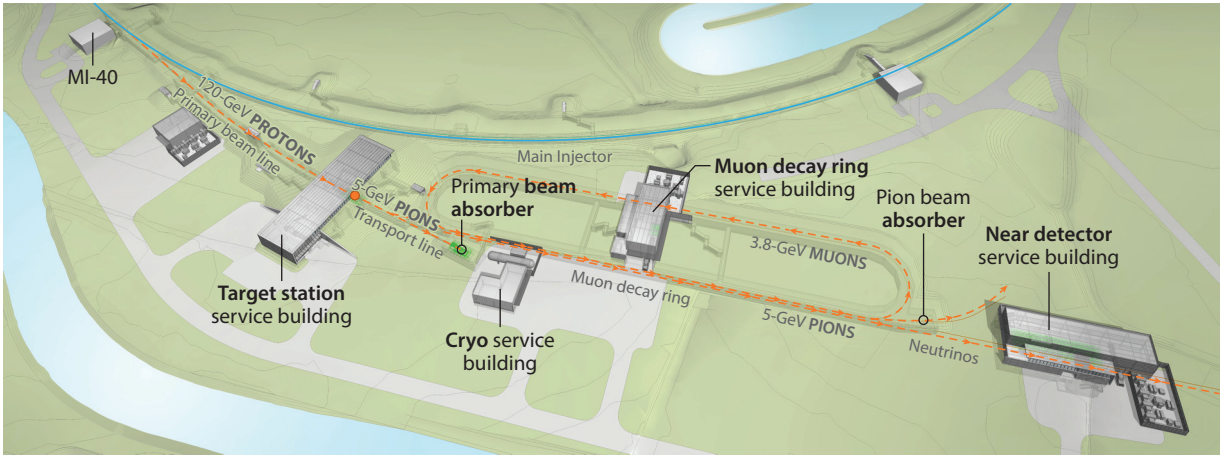


**Figure 5**

Engineering layout of the nuSTORM facility components showing the proton beam line from the Fermilab Main Injector, target station, pion transport line, decay ring, and near detector hall.

**$\beta$ function:** function related to the transverse size of a beam along its trajectory

for nuSTORM has been done, however. From the downstream end of the horn, the nuSTORM beam system is no longer similar to NuMI or any other conventional neutrino beam. From the downstream end of the horn, pion transport is continued with several radiation-hard (MgO-insulated) quadrupoles. Although conventional from a magnetic field point of view, the first two to four quadrupoles need special and careful treatment in their design in order to maximize their lifetime in this high-radiation environment. Quadrupole magnets meeting the nuSTORM radiation-resistance criteria have been successfully built and operated, however (90). The pion beam is brought from the target station and transported through a chicane section to the injection OCS of the decay ring. **Figure 6** shows a G4Beamline (91) depiction of the pion transport line and the beginning of the decay ring FODO straight section. The decay ring straight-section FODO cells were designed to efficiently transport both the 5.0 GeV/ $c$  injected pion beam and the 3.8 GeV/ $c$  circulating muon beam produced from the pion decay in the first straight section of the ring. This goal was accomplished by simultaneously optimizing the  $\beta$ functions for both beams.

A large dispersion ( $D_x$ ) is required at the injection point in order to achieve pion and muon orbit separation, which for the OCS design provides a 40-cm separation. **Figure 7** presents a

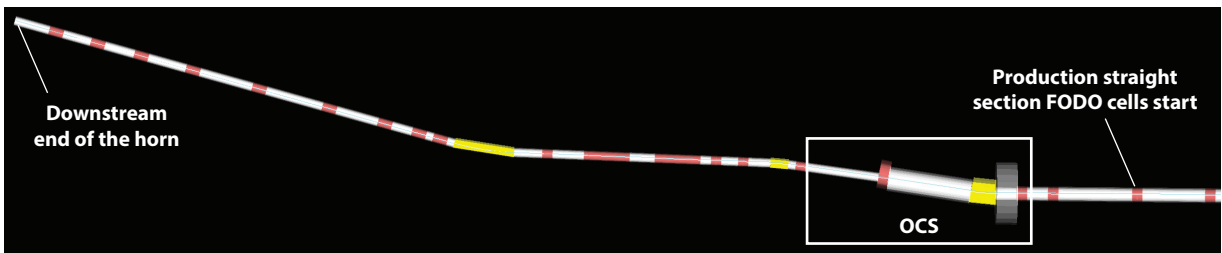


**Figure 6**

The G4 beam line drawing from the downstream face of the horn to the FODO cells. Red, quadrupole; yellow, dipole; white, drift. Abbreviation: OCS, orbit combination section.



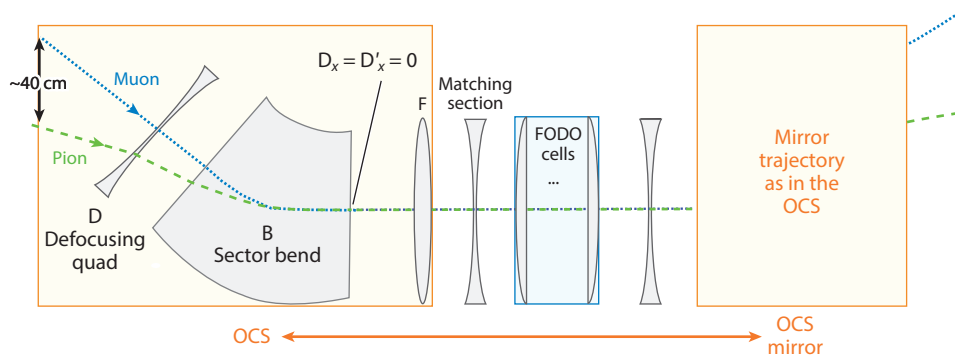


**Figure 7**

Schematic of the injection elements. Abbreviation: OCS, orbit combination section.

schematic drawing of the injection elements. The sector dipole for muons in the OCS has an entrance angle for pions that is nonperpendicular to the edge, and the defocusing quadrupole in the OCS for muons is a combined-function dipole for the pions, with both entrance and exit angles nonperpendicular to the edges. The OCS will be followed by a short matching section to the decay ring FODO cells. The performance of the injection scenario was determined by calculating the number of muons at the end of the “production” straight section [the decay ring straight section along which the detector halls are placed (**Figure 4**)] using a G4beamline simulation. In this simulation, 0.012 muons per proton on target (POT) were obtained (**Figure 8a**). These muons have a wide momentum range (beyond that which the ring can accept,  $3.8 \text{ GeV}/c \pm 10\%$ ) and thus are only partially accepted by the ring. Within the acceptance of the decay ring, approximately 0.008 muons per POT are delivered with this design. The muon beam at the end of the production straight section (first turn) is large, with  $\sigma_{x,y} \simeq 10 \text{ cm}$ . **Figure 8b** shows the time structure of the muons, which is essentially the time structure of the protons in one bunch in the MI.

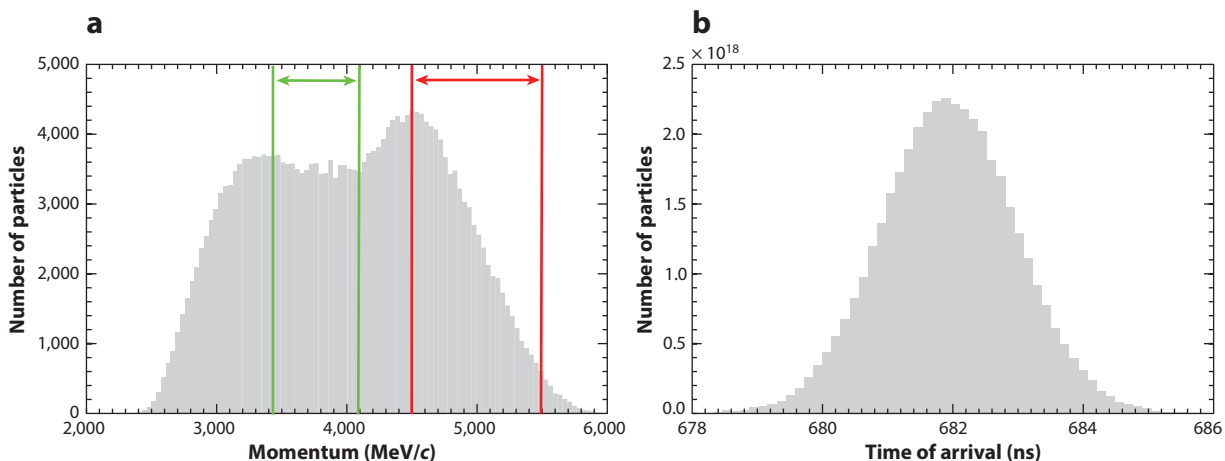


**Figure 8**

(a) The muon momentum distribution at the end of decay straight section. The green band is the  $3.8 \text{ GeV}/c \pm 10\%$  acceptance of the ring. The red band indicates the muons that are extracted by the orbit combination section mirror along with the pions. (b) Time structure of muons at the end of the decay straight section.

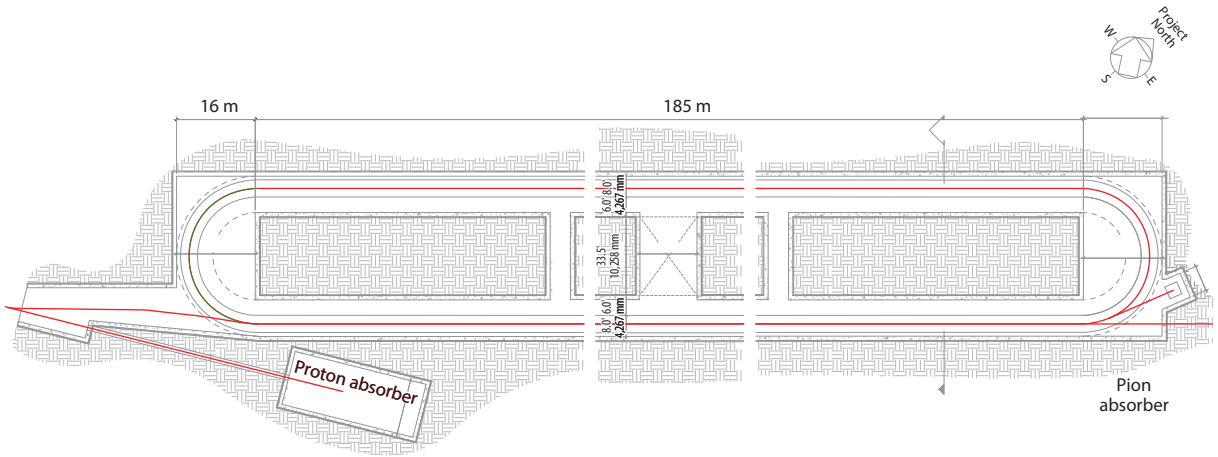


**Figure 9**

Racetrack ring layout. Pions are injected into the ring from the left. The pions and muons extracted at the end of the production straight section are transported to the pion absorber. The residual proton beam absorber location is also shown.

### 3.1. Decay Ring

The nuSTORM decay ring design (92, 93, 93a) is a compact racetrack (480 m in circumference) based on large-aperture (60-cm), separate function magnets (dipoles and quadrupoles). The ring is configured with FODO cells combined with double-bend achromat (DBA) optics. **Figure 9** illustrates the ring layout, including the injection and extraction points (OCS and OCS mirror), primary proton beam absorber, and pion beam absorber, and provides the ring design parameters. With the 185-m length of the production straight section,  $\sim 48\%$  of the pions decay before reaching the arc. Because the arcs are set for the central muon momentum of  $3.8 \text{ GeV}/c$ , the pions remaining at the end of the straight section will not be transported by the arc, making it necessary to guide the remaining pion beam to an appropriate absorber. Another OCS, which is simply a mirror reflection of the injection OCS, is placed at the end of the production straight to extract the remaining pions toward the absorber. However, the OCS mirror extracts both the residual pions and the muons that are in the same  $5 \pm 0.5 \text{ GeV}/c$  momentum range (**Figure 8**). The pions are absorbed in the absorber, but these extracted muons can be used to produce an intense low-energy muon beam (see Section 3.2). In addition to the FODO design described above, a decay ring for nuSTORM based on a racetrack, fixed-field, alternating-gradient (RFFAG) magnetic lattice, which could considerably increase (by approximately by a factor of two) the neutrino flux, is also being considered (94–96).

### 3.2. Low-Energy Muon Beam

Section 3.1 describes the OCS and its use for pion injection and extraction. As mentioned in that section, muons that are in the same momentum band ( $5 \pm 0.5 \text{ GeV}/c$ ) at the end of the production straight section will be extracted along with the pions by the mirror OCS. The beam absorber for pions can function as a muon “degrader,” if the absorber depth is appropriately chosen. An absorber depth of 3.5 m effectively absorbs all the pions while also functioning as a muon degrader to produce an intense, pulsed low-energy muon source. Results of a G4Beamline simulation are shown in **Figure 10**, which presents the energy distribution of muons exiting the downstream

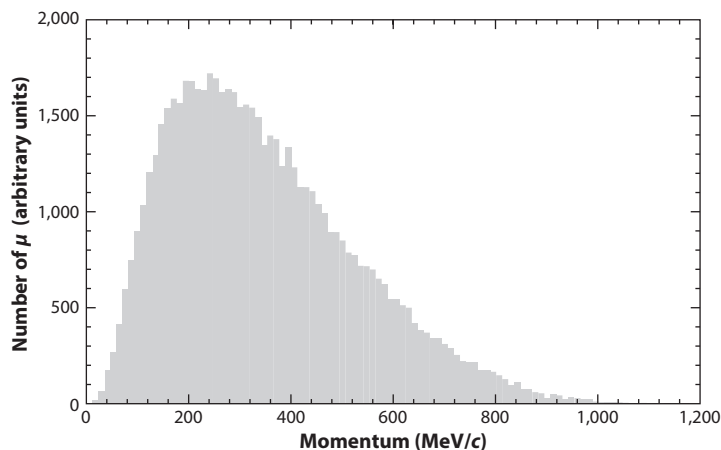


**Figure 10**

Momentum distribution of muons that exit the downstream face of the pion absorber.

face of this beam absorber. Approximately  $10^{11}$  low-energy muons are produced per MI booster batch or  $\sim 1.2 \times 10^9$  per MI bunch (**Figure 8**).

### 3.3. Beam Instrumentation

The goal of the beam instrumentation for nuSTORM is twofold. First, the instrumentation is needed to determine the neutrino flux at the near and far detectors with an absolute precision of  $<1\%$ . Both the number of neutrinos and their energy distribution must be determined. If both the circulating muon flux in the storage ring is known on a turn-by-turn basis and the orbit and orbit uncertainties (uncertainty on the divergence) are known accurately, then the neutrino flux and energy spectrum can be predicted with equal precision. The goals for the suite of beam instrumentation diagnostics for the nuSTORM decay ring are summarized as follows:

1. Measure the circulating muon intensity (on a turn-by-turn basis) to 0.1% absolute.
2. Measure the mean momentum to 0.1% absolute.
3. Measure the momentum spread to 1% (full width at half maximum).
4. Measure the tune to 0.01.

Second, from the accelerator standpoint, in order to commission and run the decay ring, turn-by-turn measurements of the following parameters are crucial: trajectory, tune, beam profile, and beam loss. The current estimates for these requirements are summarized in **Table 2**.

In order to measure the circulating muon intensities, one option is to use toroid-based fast beam-current transformers (FBCTs), such as the one recently developed at CERN for L4 (97). It consists of a one-turn calibration winding and a 20-turn secondary winding, wound on a magnetic core and housed in a four-layer shielding box. The mechanical dimensions will have to be adapted to the large beam pipe of nuSTORM. Note that obtaining an absolute precision of 0.1% will be challenging, given that problems associated with pulsed calibration and with electromagnetic interference (EMI) will influence the absolute accuracy of the FBCT. However, all components of the nuSTORM decay ring are dc, which will help with regard to EMI, but measurements on nonstable beams could become problematic. Demonstration of FBCTs that operate with nonstable beams and are not affected by daughter particles from the decay is one of the few R&D tasks required for the technical implementation of nuSTORM. A combination of FBCT design, location

**Table 1** Decay ring specifications<sup>a</sup>

| Parameter                     | Specification        | Unit       |
|-------------------------------|----------------------|------------|
| Central momentum ( $P\mu$ )   | 3.8                  | GeV/ $c$   |
| Momentum acceptance           | $\pm 10\%$           | Full width |
| Circumference                 | 480                  | m          |
| Straight section length       | 185                  | m          |
| Arc length                    | 55                   | m          |
| Beam-pipe diameter            | 60                   | cm         |
| Arc cell                      | Double-band achromat | NA         |
| Ring tunes ( $\nu_x, \nu_y$ ) | 9.72, 7.87           | NA         |
| Number of dipoles             | 16                   | NA         |
| Number of quadrupoles         | 128                  | NA         |
| Number of sextupoles          | 12                   | NA         |

<sup>a</sup>Abbreviation: NA, not applicable.

along the beam line and within the decay ring, and application of shielding is the proposed R&D approach.

#### 4. DETECTOR DESIGN FOR THE nuSTORM NEUTRINO PHYSICS PROGRAMS

Any of the multipurpose detectors being considered as near detectors for the next generation of LBL experiments will meet the physics requirements for the detectors needed for the neutrino interaction physics program at the near hall at nuSTORM, or for the detector needed as part of an SBL oscillation physics program; they are described in detail elsewhere (98, 99). The far detector, at  $\simeq 2,000$  m, is used for the SBL neutrino oscillation physics studies and requires some special capabilities in order to maximize its performance for searches in both the neutrino appearance and disappearance channels accessible at the nuSTORM facility.

The SBL element of the nuSTORM physics program would utilize the so-called golden channel (in Neutrino Factory parlance), in which a neutrino oscillation appearance signal is given by the observation of a “wrong-sign” muon in the signal event. For example, with  $\mu^+$  stored in the ring ( $\nu_e$  and  $\bar{\nu}_\mu$  production), the oscillation of  $\nu_e \rightarrow \nu_\mu$  can produce a  $\nu_\mu$  charged-current (CC) interaction in the detector that will have a  $\mu^-$  in the final state, which is a muon with the wrong sign versus that expected from the CC interactions of the  $\bar{\nu}_\mu$  in the beam. This detector needs to

**Table 2** Decay ring instrumentation specifications for circulating muons<sup>a</sup>

|                 | Absolute accuracy | Resolution |
|-----------------|-------------------|------------|
| Intensity       | 0.1%              | 0.01%      |
| Beam position   | 5 mm              | 1 mm       |
| Beam profile    | 5 mm              | 1 mm       |
| Tune            | 0.01              | 0.001      |
| Beam loss       | 1%                | 0.5%       |
| Momentum        | 0.5%              | 0.1%       |
| Momentum spread | 1%                | 0.1%       |

<sup>a</sup> $\simeq 10^9$  per Main Injector bunch.

be magnetized in order to determine the sign of the muon. A magnetized iron detector similar to that used in MINOS was considered the most straightforward and cost-effective approach for SBL neutrino oscillation physics. Thus, for the purposes of the nuSTORM oscillation physics, a detector inspired by MINOS (100), but with thinner plates and a much larger excitation current (a larger B field), was used as the baseline concept. The detector is an iron and scintillator sampling calorimeter called SuperBIND (Super B Iron Neutrino Detector) (1), and it has a cross section of 6 m (diameter) in order to maximize the ratio of the fiducial mass (1.3 kt) to total mass. The magnetic field will be toroidal, as in MINOS, and will use extruded scintillator for the readout planes. However, SuperBIND will use superconducting transmission lines (STLs) to carry the excitation current and thus will allow for a much larger B field in the steel ( $\sim 2$  T or greater over almost all of the steel plate). **Figure 11** presents an overall schematic of the detector. The STL concept was developed for the Design Study for a Staged Very Large Hadron Collider (101), but recent cable-in-conduit superconductor developments that have been carried out for ITER (102–104) will be applicable to the SuperBIND design. Minimization of the muon charge misidentification rate requires the highest field possible in the iron plates; thus, SuperBIND will require a much larger (240 kA-turns) excitation current than even that of the MINOS near detector (40 kA-turns). The excitation circuit for SuperBIND consists of eight turns, each carrying 30 kA (**Figure 11**).

## 5. PERFORMANCE OF THE nuSTORM FACILITY: NEUTRINO PHYSICS

The reach of the neutrino physics that can be done at the nuSTORM facility is determined, to a large degree, by the quality of the neutrino beams it produces. The nuSTORM facility provides

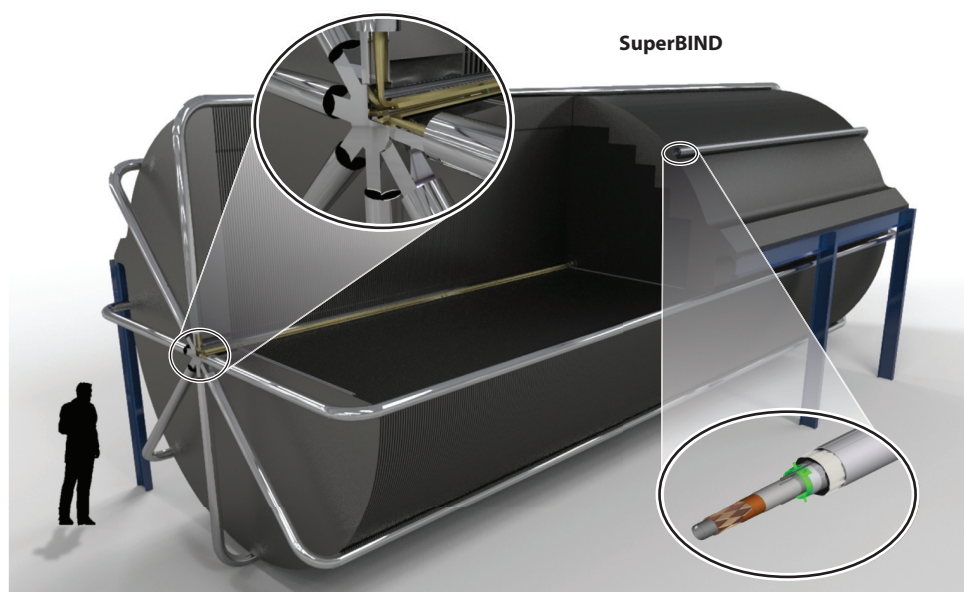


**Figure 11**

Far detector concept. (*Left inset*) The central cryostat with eight return loops. (*Right inset*) Detail of the superconducting transmission line.

bright, flavor-pure beams that can be precisely characterized by beam instrumentation in the pion transfer line and in the decay ring. This property is what sets nuSTORM apart from other neutrino sources, giving it many of the qualities of a photon light source (accurate flux and energy determination). The physics program that can be done at the near hall at nuSTORM is identical to that being proposed at the near sites of planned future LBL oscillation experiments (T2HK and LBNE, for example) and could use similar, if not identical, detector systems. However, with respect to neutrino interaction physics, nuSTORM provides large samples of  $\nu_e$  and  $\bar{\nu}_e$  beams as well as nearly flavor-pure  $\nu_\mu$  and  $\bar{\nu}_\mu$  beams. For the SBL oscillation physics performance, nuSTORM takes advantage of the golden channel (appearance) mentioned above and has access to the  $\bar{\nu}_\mu^{(-)}$  disappearance channels. The  $\bar{\nu}_e^{(-)}$  appearance and disappearance channels would be most effectively studied with a magnetized totally active detector such as liquid argon.

## 5.1. Neutrino Beams Produced at nuSTORM

As mentioned in Section 1, the neutrino beams produced at nuSTORM can be characterized with excellent precision with the use of conventional beam diagnostic instrumentation to understand the parent particle distributions, from which the neutrino flux can then be precisely calculated. In the following subsections, we describe the neutrino beams expected from the facility (105), indicating the overall flux (normalized to  $10^{21}$  POT), neutrino flavor composition, and expected bin-to-bin errors.

**5.1.1. Neutrino flux from the pion beam.** Although the design case of nuSTORM is to produce neutrinos from muon decay, the neutrino beam from pion decay in the production straight section produces a very intense  $\bar{\nu}_\mu^{(-)}$  beam. In order to quantitatively investigate this beam, an ensemble of particles produced in a MARS (106) simulation of the target and horn were tracked using G4Beamline from the downstream face of the horn through the transfer line and injection into the decay ring via the OCS. After tracking through the transfer line, the pion beam was sampled at 50 locations along the production straight section to yield an ensemble of pions representative of the beam. To obtain the muon ensemble, the pions were allowed to decay and the muons were sampled at the end of the production straight section, weighted for the momentum acceptance of the ring.

The sampling of the particles' energy and momenta in the G4Beamline tracking could then be used to calculate (from decay kinematics) the neutrino flux at arbitrary locations, or G4Beamline could be used to simulate the production of the neutrino beam itself. This sampling is considered to be analogous to the information of the beam obtained from standard diagnostic instrumentation.

The simulated flux from a  $\pi^+$  beam, which included all particle types transported from the target to the ring (pions, kaons, muons) at the near detector, is depicted in **Figure 12a**, and the flux at the 2-km far detector is shown in **Figure 12b**. Here, due to the statistical limitations of the full G4Beamline tracking to observe suppressed decay branches, the flux was calculated from the pion and kaon distributions, allowing for all possible decay branches. The figure demonstrates that nuSTORM produces a  $\nu_\mu$  beam of unmatched purity. Although not shown in **Figure 12**, the simulation did include the neutrino flux from  $K^+ \rightarrow \nu_e$ ,  $\pi^- \rightarrow \bar{\nu}_\mu$ , and  $\pi^+ \rightarrow \nu_e$ . Their contribution to the flux was too small to be observed on the scale depicted.

**5.1.2. Muon beam.** By use of the same methodology of simulating the particle trajectories of the pions within the decay straight section, a sample of muons was obtained from which the neutrino flux at arbitrary detector locations could be determined. The errors on the binned flux

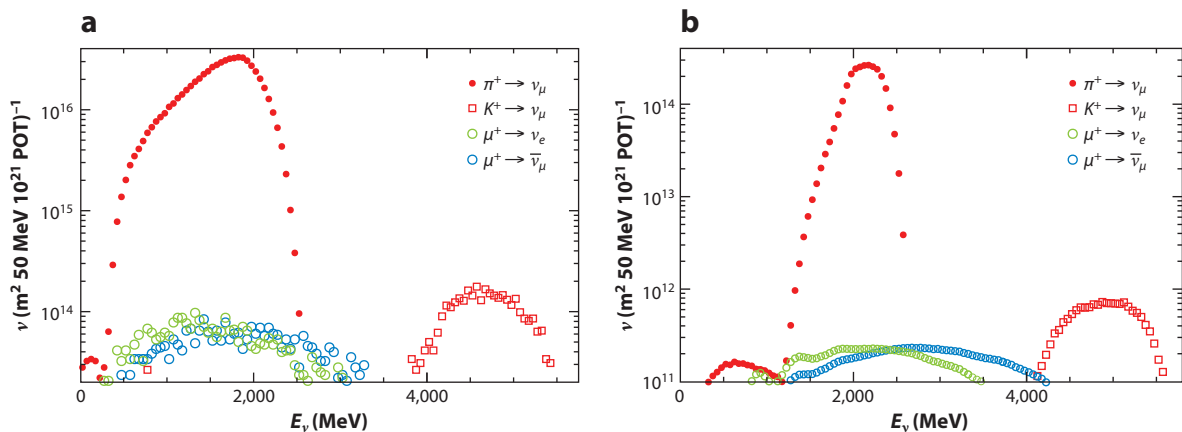


Figure 12

Neutrino flux from the  $\pi^+$  beam (a) at the near detector and (b) at the far detector. Abbreviation: POT, protons on target.

depend solely on the knowledge of the particle trajectories obtained by the beam diagnostics. A combination of instrumentation performance predictions and simulations imply that the bin errors will be below 1% (Table 3). The simulated flux from the stored  $\mu^+$  beam for the near detector is shown in Figure 13a, and that for the 2-km far detector is shown in Figure 13b.

**5.1.3. Neutrino flux precision.** The precision of the flux estimates is affected by several factors, including understanding and stability of the magnetic lattice, the overall flux of and type of particles transported by the lattice, and the momentum distributions of those particles. Given the time structure of the beam and the bunch intensity, in the absence of particle decays, BCTs can measure the circulating beam intensity (or, in the case of pions, the intensity in the production straight section) to a precision approaching 0.1%. Determining, quantitatively, the effects of particle decays on the BCTs still needs to be done and is considered one of the few R&D tasks needed in order to implement nuSTORM. In order to investigate the effect of a measurement error on the divergence of the muons stored in the ring, the muon divergence of each particle in the muon beam was inflated by 2% and the resulting flux was compared with the nominal divergence. The mean difference in the flux in 50-MeV energy bins based on a 2% error in the divergence of the primary beam was determined to be  $\simeq 0.6\%$ .

**5.1.4. Rates.** On the basis of the flux calculations given above, the number of neutrino interactions expected from a total exposure of  $10^{21}$  POT was calculated and is given in Table 4 for a 100-T detector at 50 m. Table 5 provides the number of CC interactions in the far detector (1.3-kt

Table 3 Flux uncertainties expected for nuSTORM

| Parameter     | Uncertainty    |
|---------------|----------------|
| Intensity     | 0.3%           |
| Divergence    | 0.6%           |
| Energy spread | 0.1%           |
| Total         | $\lesssim 1\%$ |



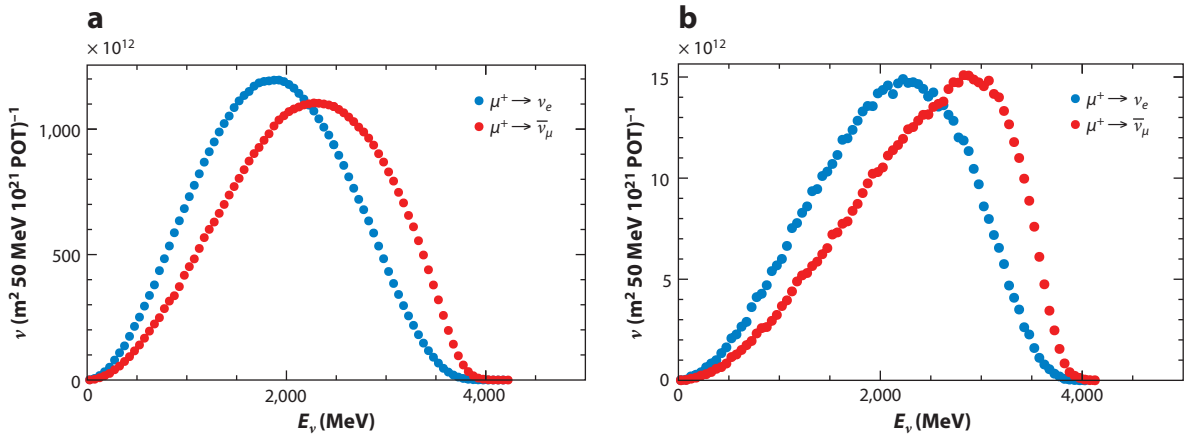


**Figure 13**

Neutrino flux from  $\mu^+$  decay (a) at the near detector and (b) at the far detector. Abbreviation: POT, protons on target.

fiducial mass) for a null-oscillation assumption and for the case where a  $3 + 1$  model with the LSND/MiniBooNE best-fit parameters is assumed.

## 5.2. nuSTORM's Sensitivity to Sterile Neutrinos

The nuSTORM facility provides the opportunity to perform searches for sterile neutrinos with unmatched sensitivity and breadth. In this section, we review the analysis for the  $\bar{\nu}_\mu$  appearance and disappearance channels that was performed using the beams ( $\mu^+$  stored) normalized to  $10^{21}$  POT and using the SuperBIND detector described in the previous section. The performance estimates are based on a detailed simulation in which neutrino events in SuperBIND were generated using GENIE (version 2.8.4) (107). The interaction products were propagated through the detector using GEANT4 (version 10.00) (108), and the resulting energy deposition was smeared with a simple digitization algorithm and clustered into hits. Finally, a reconstruction optimized for the identification of muon tracks associated with neutrino CC interactions was applied to the digitized simulation.

The reconstruction used a simple geometric approach to identify potential tracks, as well as a Kalman filter algorithm to extend the track to the event vertex and to fit for the curvature

**Table 4** Event rates at 50 m from the end of the decay straight section per 100 T for  $10^{21}$  POT<sup>a</sup>

| $\mu^+$ stored channel   | $10^3$ events | $\mu^-$ stored channel   | $10^3$ events |
|--------------------------|---------------|--------------------------|---------------|
| $\nu_e$ CC               | 5,188         | $\bar{\nu}_e$ CC         | 2,519         |
| $\bar{\nu}_\mu$ CC       | 3,030         | $\nu_\mu$ CC             | 6,060         |
| $\nu_e$ NC               | 1,817         | $\bar{\nu}_e$ NC         | 1,002         |
| $\bar{\nu}_\mu$ NC       | 1,174         | $\nu_\mu$ NC             | 2,074         |
| $\pi^+$ injected channel | $10^3$ events | $\pi^-$ injected channel | $10^3$ events |
| $\nu_\mu$ CC             | 41,053        | $\bar{\nu}_\mu$ CC       | 19,939        |
| $\nu_\mu$ NC             | 14,384        | $\bar{\nu}_\mu$ CC       | 6,986         |

<sup>a</sup>Abbreviations: CC, charged current; NC, neutral current; POT, proton on target.

**Table 5** Event rates due to CC interactions at 2 km per 1.3 kt for  $10^{21}$  POT<sup>a</sup>

| $\mu^+$ stored                            |                |             |
|---|----------------|-------------|
| Channel                                   | No oscillation | Oscillation |
| $\nu_e \rightarrow \nu_\mu$               | 0              | 288         |
| $\nu_e \rightarrow \nu_e$                 | 188,292        | 176,174     |
| $\bar{\nu}_\mu \rightarrow \bar{\nu}_\mu$ | 99,893         | 94,776      |
| $\bar{\nu}_\mu \rightarrow \bar{\nu}_e$   | 0              | 133         |
| $\pi^+$ stored                            |                |             |
| Channel                                   | No oscillation | Oscillation |
| $\nu_\mu \rightarrow \nu_\mu$             | 915,337        | 854,052     |
| $\nu_\mu \rightarrow \nu_e$               | 0              | 1,587       |

<sup>a</sup>Abbreviations: CC, charged-current; POT, proton on target.

(109). **Figure 14** shows the reconstruction and charge identification efficiency of this algorithm for  $\nu_\mu$  CC interactions in SuperBIND. Multiple trajectories are identified by reconstruction, and the longest is identified as the muon. Despite this, a number of events will be identified with the incorrect charge, either from failures in the reconstruction algorithm or from pions that are misidentified as muons. The fractional occurrence of such events is the complement of the charge identification efficiency shown in **Figure 14**. Such tracks are the primary background for the identification of muon-flavored CC neutrino interactions in both the wrong-sign appearance and disappearance channels. The analysis described here utilized the Toolkit for Multi-Variate Analysis (TMVA) (110), included as part of the ROOT package (111). The analysis was optimized for signal significance given an initial sample size of signal and background events calculated using the GloBeS program (112) with sterile neutrino parameters derived from recent global fits (65) to SBL appearance data, assuming a  $3 + 1$  sterile neutrino model.

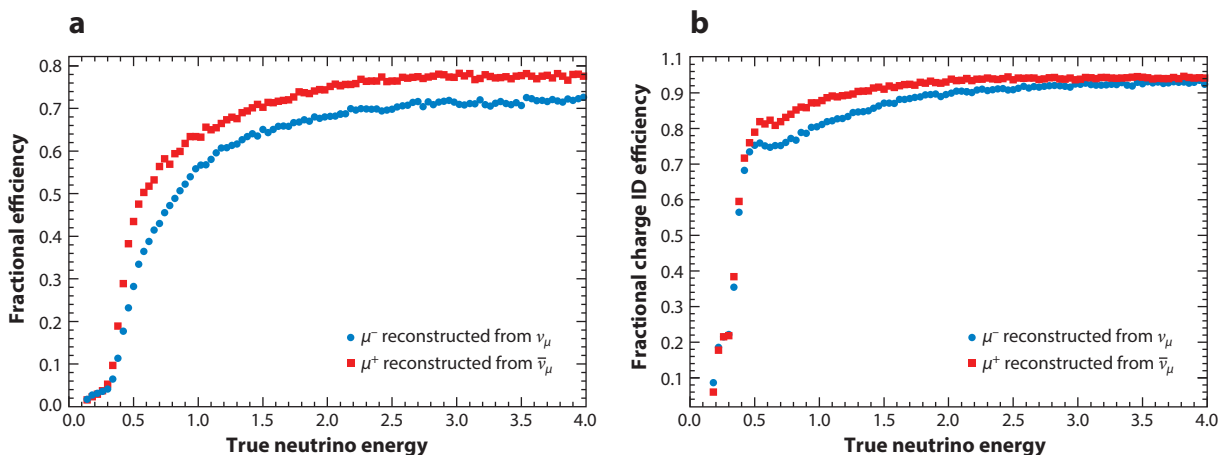


**Figure 14**

(a) Reconstruction and (b) charge identification (charge ID) efficiencies for muons generated from charged-current neutrino interactions in SuperBIND, at typical nuSTORM energies.

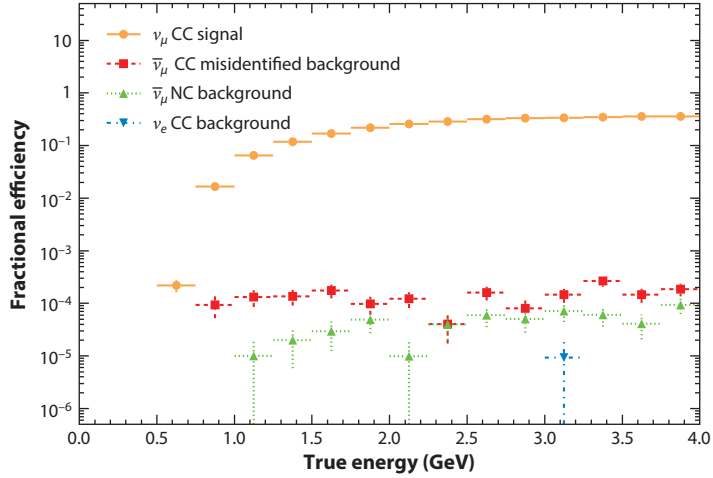


**Figure 15**

Event selection efficiency of the optimized boosted decision tree analysis for SuperBIND, at the energies available to the nuSTORM facility. Abbreviations: CC, charged-current; NC, neutral-current.

**5.2.1. Sterile neutrino oscillation physics with muon neutrinos: appearance and disappearance channels.** The optimization of the  $\nu_\mu$  appearance channel was conducted using the significance statistic  $S/\sqrt{S+B}$ , where  $S$  is the total number of selected signal events and  $B$  is the number of background events selected. Several different multivariate methods were tested for this analysis, but the boosted decision tree (BDT) method produced the best result. **Figure 15** shows the fraction of events that survived the application of the BDT analysis on sets of neutrino CC and neutral-current (NC) events, as a function of the true neutrino energy. The resultant signal efficiency is reduced in this optimization in order to reduce the background below the level of a few parts in  $10^4$ . This degree of background suppression is what enables a measurement in this channel with the potential for  $10\sigma$  sensitivity.

The sensitivity for  $\nu_e \rightarrow \nu_\mu$  (the  $CPT$ -invariant channel of the LSND/MiniBooNE signal) was determined within the GLoBeS framework. The simulation provided the detector response, as characterized in a so-called migration matrix that maps the true neutrino interaction rates to reconstructed neutrino rates, including both efficiency and resolution effects. The migration matrix was then used as input to the GLoBeS program. The signal ( $\nu_\mu$  CC) response was evaluated with the background ( $\nu_e$  CC,  $\bar{\nu}_\mu$  CC,  $\bar{\nu}_\mu$  NC) response, and the number of events in each associated channel was evaluated for the potential values of  $\Delta m_{14}^2$  between 0.03 and 30  $\text{eV}^2$  and  $\theta_{e\mu}$  between  $10^{-6}$  and 0.1. A representation of the deviation from the null-oscillation hypothesis was then calculated using a  $\chi^2$  statistic for each point, and the result was then used to map out the sensitivity shown in **Figure 16**. This sensitivity is plotted with contours determined from global fits (**Figure 2**) to the existing SBL neutrino oscillation appearance data, including LSND, MiniBooNE, ICARUS, and MINOS. The  $10\sigma$  significance contour demonstrates that the  $\nu_\mu$  appearance measurement alone will provide a definitive statement regarding the existence of a sterile neutrino in the region consistent with the global fit to the LSND, MiniBooNE, gallium, and reactor data. Further measurements will refine these results.

The muon disappearance channel used a similar analysis with a different optimization. The disappearance measurement is an analysis of the spectrum shape, so a pure counting statistic is insufficient. A  $\chi^2$  was adopted as a figure of merit to determine the largest separation between

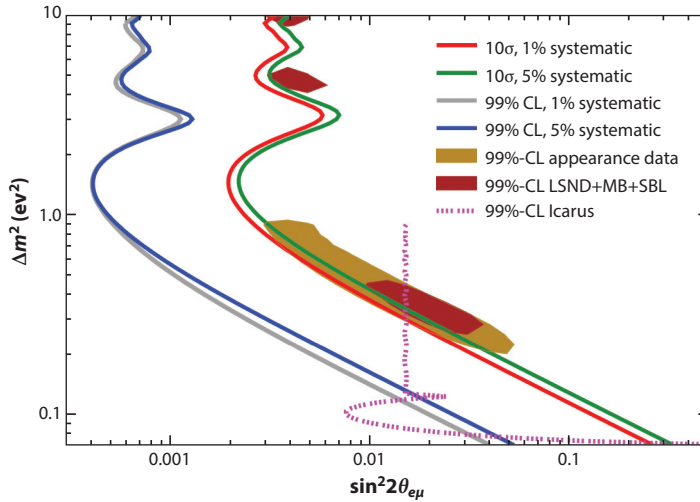


**Figure 16**

The sensitivity of a  $\nu_\mu$  appearance experiment to a short-baseline oscillation due to a sterile neutrino, assuming a  $3 + 1$  model. Both the  $10\sigma$  significance and 99%-CL contours are shown for two different scenarios for the systematic uncertainties: one in which the total systematic uncertainty is 1% of the beam normalization and a second in which the systematic uncertainty is 5%. The 99% contour generated from the fit to the MiniBooNE (MB) and LSND experiments with the gallium and reactor anomalies is represented by the brown areas, and the fit to all available appearance data is represented by the tan area. The recent 99% exclusion contour from Icarus is also shown.

the null hypothesis and a test case, before compiling the sensitivity curves of  $\Delta m_{14}^2$  versus  $\theta_{\mu\mu}$  (**Figure 17**), where

$$\sin^2 2\theta_{\mu\mu} = 4|U_{\mu 4}|^2(1 - |U_{\mu 4}|^2). \quad 2.$$

These curves were again compiled using GloBeS with the response from the signal ( $\bar{\nu}_\mu$  CC) and background ( $\bar{\nu}_\mu$  NC and  $\nu_e$  CC) simulations. The 99%-CL limits from the disappearance measurement with a muon decay source can provide an improvement over the limits from existing data for  $\Delta m_{14}^2$  greater than  $0.3 \text{ eV}^2$ . Assuming a total systematic uncertainty of 1%, nuSTORM has the potential for a discovery with  $5\sigma$  significance in the region allowed by the current exclusion limits.

The  $\nu_\mu$  flux from pion ( $\pi^+$  injected) decay is 13 times greater than the neutrino flux from muon decay in nuSTORM and has a very different energy distribution. The information provided by the  $\nu_\mu$  disappearance channel is complementary to that from the  $\bar{\nu}_\mu$  disappearance channel. The  $\nu_\mu$  disappearance experiment was simulated using an optimization similar to that of the  $\bar{\nu}_\mu$  disappearance experiment and the neutrino flux shown in **Figure 12**. The contour showing the  $5\sigma$  CL for a measurement at nuSTORM with this pion neutrino source as a function of  $\Delta m_{14}^2$  versus  $\sin^2 2\theta_{\mu\mu}$  is shown in **Figure 17b**. Because of the narrower energy distribution in the pion source, there is a larger variation in the limits as a function of  $\Delta m_{14}^2$ . However, there is still potential for improvement over existing limits for a large subset of  $\Delta m_{14}^2$  greater than  $0.3 \text{ eV}^2$ .

**5.2.2. Global fits to the muon neutrino channels.** The combination of the disappearance and appearance measurements is an important feature of nuSTORM, as measurements of multiple channels can be made simultaneously. A fit using the combination of the signal channels, such as the  $\nu_\mu$  appearance and  $\bar{\nu}_\mu$  disappearance channel from the muon decay source and the  $\nu_\mu$  disappearance

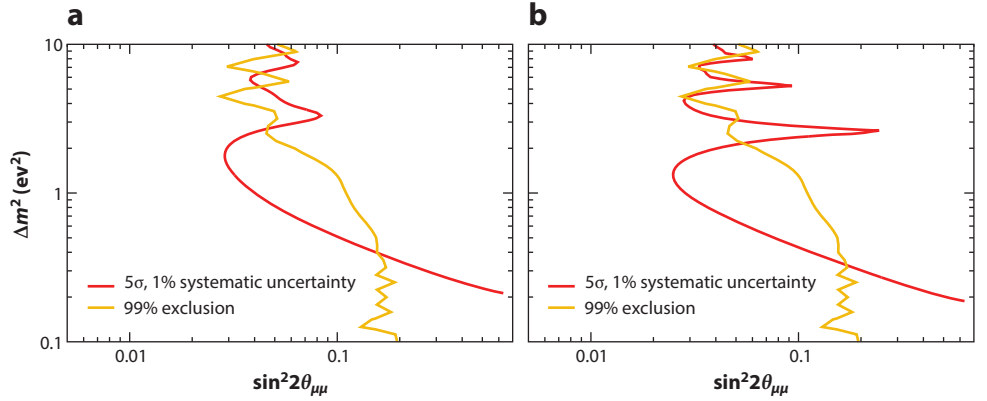


**Figure 17**

The sensitivity of (a) a  $\bar{\nu}_\mu$  from  $\mu^+$  decay and (b) a  $\nu_\mu$  from  $\pi^+$  decay disappearance experiment to a short-baseline neutrino oscillation due to a sterile neutrino, assuming a 3+1 model. The  $5\sigma$  contour for the disappearance experiment for a 1% systematic uncertainty is shown, along with the 99% exclusion limit derived from the existing disappearance oscillation data.

channel from the pion decay source, is allowed because the channels are not statistically correlated; any correlation between individual events because of a shared source decay is lost due to the low neutrino interaction rate. The channels from the muon decay source are separated by charge, and the pion decay source is separated from the muon decay source by time. This additional information reduces the number of assumptions required by the fit to the data for a given sterile neutrino model. **Figure 18** shows the improvement in the measurement of  $\theta_{e\mu}$  and  $\theta_{\mu\mu}$  from the combination of multiple channels. The addition of disappearance information produces an improvement in the appearance sensitivity at  $\Delta m_{14}^2 \sim 1 \text{ eV}^2$ , but leads to minimal improvement in the region preferred by existing measurements. In contrast, the addition of the appearance measurement makes a minimal contribution to contours in the  $\theta_{\mu\mu}$  plane, whereas the combination of the two disappearance measurements results in a substantial increase in the coverage.

**5.2.3. Sterile neutrino oscillations with electron neutrinos.** Although a strong case can be made for nuSTORM using only the  $\nu_\mu$  oscillation physics, it is also important to measure oscillations to  $\mu_e$ s to evaluate the consistency of any measurement. SuperBIND is not optimized for the measurement of  $\mu_e$  interactions, because single electrons cannot be resolved for charge identification, nor may the interaction vertex be positively inferred. However, an electron shower may be observed in SuperBIND, and a figure of merit may be defined on the basis of the distribution and extent of photoelectrons observed in the detector, which can differentiate (with high purity)  $\mu_e$  interactions from NC interactions (which are the leading background). In order to achieve this high purity, hard cuts were imposed on the observed shower shape and deposited charge, such that the detection efficiency for  $\mu_e$  CC events is reduced to 10%. The corresponding NC background rejection factor is 99.7%. The cut on the figure of merit was tuned to minimize the number of NC events identified as  $\mu_e$  CC events while maintaining a high enough  $\nu_e$  CC efficiency to produce a useful number of candidate events. Of the three  $\mu_e$  oscillation channels, only the  $\nu_\mu \rightarrow \nu_e$  channel available from the pion decays may produce a significant measurement in SuperBIND on the basis of these efficiencies.

In the context of the pion-sourced neutrino beam, the backgrounds for the  $\nu_\mu \rightarrow \nu_e$  appearance channel are from unoscillated  $\nu_\mu$  as well as from  $\bar{\nu}_\mu$  and  $\nu_e$  from muon decays in the first 1.6 ns

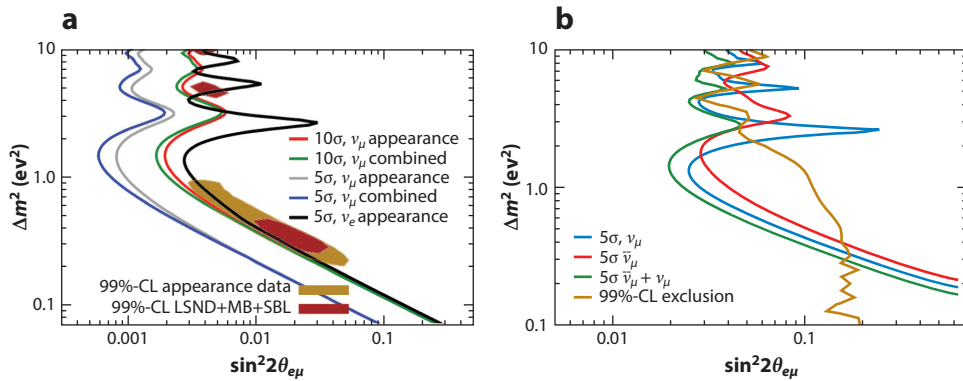


**Figure 18**

Sensitivities of combinations of experiments at nuSTORM to short-baseline (SBL) neutrino oscillations associated with a sterile neutrino assuming a 3+1 model. (a) The combination of  $\nu_\mu$  appearance and disappearance experiments expressed in terms of the effective mixing angle  $\theta_{e\mu}$ . Included is the  $5\sigma$  contour derived from the  $e$  appearance data from the pion beam source. (b) The sensitivity of the  $\nu_\mu$  disappearance experiment from the pion decay source and the  $\bar{\nu}_\mu$  disappearance experiment from the muon decay source as  $5\sigma$  significance contours. The green line represents the sensitivity of the combination of the experiments.

after injection. The  $\bar{\nu}_\mu^{(-)}$  CC interactions may be clearly distinguished from NC interactions by the presence of a muon, so further suppression of more than an order of magnitude may be expected over the above  $\mu_e$  selection. There is nothing to distinguish the beam  $\nu_e$  from the oscillated  $\nu_e$ , so no further suppression is possible for this background. Even so, a  $5\sigma$  measurement may be made in the region favored by the LSND and MiniBooNE data (**Figure 18a**). This measurement will not make a substantial contribution to the global fit of the nuSTORM channels because of its relatively low overall significance.

Given that the experiment is not limited by systematic uncertainties in the beam composition, great gains in  $\bar{\nu}_e^{(-)}$  appearance measurements can be made with increased detector resolution and efficiency. A more significant measurement of SBL  $\nu_e$  appearance from pion decays may be possible with a greater signal efficiency for  $\nu_e$  CC interactions with better background rejection. To achieve the  $10\sigma$  significance observed in the  $\nu_\mu$  appearance, the background must be suppressed by a factor of  $10^{-4}$  with respect to the signal. Once such a suppression factor is achieved along with a modest increase in efficiency, a measurement from  $\bar{\nu}_\mu \rightarrow \bar{\nu}_e$  appearance (generated by muon decays) may also be achieved, producing a simultaneous measurement of appearance in both neutrino charge states, similar to what is achieved with the  $\nu_\mu$  disappearance. The required  $10^{-4}$  background suppression can be achieved in a magnetized, totally active detector with strong particle identification capabilities. The strongest candidate technology is a magnetized liquid argon time-projection chamber (TPC), although it has not yet been demonstrated that the particle and charge identification capability of such a detector will provide the required background rejection (113). We note that if the existence of a light sterile neutrino is confirmed,  $CP$  violation in a 3+1 scenario might be observable in a nuSTORM-like facility (114), especially if  $\bar{\nu}_e^{(-)}$  and  $\bar{\nu}_\mu^{(-)}$  appearance and disappearance channels are accessible. A magnetized liquid argon TPC has the potential to make such observations possible.

**5.2.4. Systematics.** The experimental sensitivity obtainable at the nuSTORM facility from muon decays uses the systematic uncertainties shown in **Table 6**. These systematic uncertainties

**Table 6** Systematic uncertainties expected for a short-baseline muon neutrino appearance experiment based at nuSTORM

| Uncertainty                  | Expected contribution |            |
|------------------------------|-----------------------|------------|
|                              | Signal                | Background |
| Flux                         | 0.5%                  | 0.5%       |
| Cross section                | 0.5%                  | 5%         |
| Hadronic model               | 0                     | 8%         |
| Electromagnetic model        | 0.5%                  | 0          |
| Magnetic field               | 0.5%                  | 0.5%       |
| Variation in steel thickness | 0.2%                  | 0.2%       |
| Total                        | 1%                    | 10%        |

are motivated by the exceptionally low beam uncertainties (see Section 5.1) and expected improvements in the measurements of neutrino cross sections. With these uncertainties, the expected interaction physics uncertainty is limited by the detector performance. An upper limit on the potential systematic uncertainty is based on the existing estimates of systematic uncertainties reported by MINOS. To illustrate the effect that this limit would impose on results from nuSTORM, the systematic uncertainties were inflated by a factor of five to produce the 5% contours in **Figure 16**. Increasing the systematic uncertainty in this way has a minimal impact on the measurements of the  $\nu_\mu$  appearance due to the small number of background events surviving selection. In contrast, the significant backgrounds allowed for the disappearance measurements mean that the systematic uncertainties have a large impact on the disappearance measurements.

## 6. PATH TO A MUON COLLIDER

### 6.1. Introduction

Muons for a muon collider (115–120) are produced as a tertiary beam: Protons are directed onto a target to yield a beam of pions that are then captured in a high-field solenoid and allowed to drift and decay into muons. As a result, the muon beam has a very large phase-space size, commonly referred to as emittance. Reducing the emittance of the beam (i.e., cooling the muon beam) is required in order to reach an acceptable level of performance for the muon collider and, for the neutrino factory, can provide an increase of up to a factor of three in the neutrino flux. Given that muons have a relatively short life span ( $2.2\ \mu\text{s}$  in the rest frame), ionization cooling (121–123) is deemed to be the only technique that is fast enough to cool a muon beam without excessive loss due to decay.

### 6.2. Ionization Cooling Overview

Various aspects of muon ionization cooling were actively studied over the last two decades, first by the Neutrino Factory and Muon Collider Collaboration (NFMCC) and later by the Muon Accelerator Program (MAP; <http://www.cap.bnl.gov/mumu/>, <http://map.fnal.gov/>) (124–126). Muon-based accelerator facilities have the potential to discover and explore new fundamental physics but require the development of demanding technologies and innovative concepts. One of these is muon ionization cooling. We briefly review muon ionization cooling, starting with the fundamentals of transverse cooling.

Transverse cooling is achieved by letting a beam of muons pass through an absorber in which all components of each particle’s momentum are reduced (**Figure 19a**). The longitudinal momentum



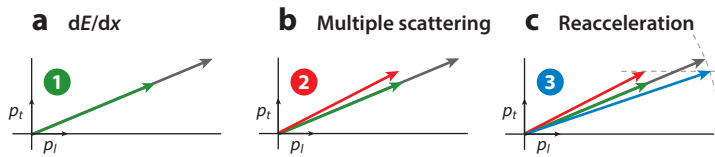


**Figure 19**

Ionization cooling principle.  $p_t$  and  $p_l$  are the transverse and longitudinal muon momentum, respectively. (a) All components of momentum are reduced in material (green arrow). (b) Multiple scattering in material increases the angular spread of the particles (red arrow). (c) Longitudinal momentum is restored in radio-frequency cavities (transition from red to blue arrow). The overall effect is that the beam spread is reduced (transition from gray to blue arrow).

is then restored in a set of radio-frequency (RF) cavities. If the absorber material and optics parameters are chosen carefully, the net effect is a reduction in the transverse emittance. However, multiple scattering in the absorber material also occurs, increasing the phase space (**Figure 19b**). After application of the RF (**Figure 19**) there is a reduction in the transverse phase space. The amount of cooling is described by the following formula:

$$\frac{d\epsilon_n}{dz} \approx -\frac{1}{\beta^2} \left\langle \frac{dE_\mu}{dz} \right\rangle \frac{\epsilon_n}{E_\mu} + \frac{1}{\beta^3} \frac{\beta_\perp E_s^2}{2E_\mu mc^2 X_0}, \quad 3.$$

where  $\beta = v/c$ ,  $\epsilon_n$  is the normalized emittance ( $\epsilon_n = \beta\gamma\epsilon$ , where  $\gamma$  is the Lorentz factor and  $\epsilon$  is the geometric emittance characterizing the size of the beam in phase space),  $z$  is the path length,  $E_\mu$  is the muon beam energy,  $X_0$  is the radiation length of the absorber material, and  $E_s$  is the characteristic scattering energy.  $\beta_\perp$  is the betatron function that relates the beam width at the location  $s$  along the nominal beam trajectory to its emittance via  $\sigma(s) = \sqrt{\epsilon \cdot \beta_\perp(s)}$ .

Equation 3 shows two competing effects: The first term is the cooling (reduction of phase-space beam size) from ionization energy loss, and the second term is heating (increase of phase-space beam size) from multiple scattering. The latter term can be minimized by reducing  $\beta_\perp$  (by placing the absorber at a minimum of the betatron function) and by choosing a low- $Z$  material to increase  $X_0$ . The so-called equilibrium emittance is the point in the cooling channel where the normalized emittance no longer changes ( $\frac{d\epsilon_n}{dz} = 0$ ) and is approximately

$$\epsilon_n^{\text{eq}} \approx \frac{\beta_\perp (0.014)^2}{2\beta m_\mu \frac{dE_\mu}{dz} X_0}. \quad 4.$$

6D cooling, reducing both the transverse and longitudinal sizes of the beam, results in the best-quality beam. In order to reduce the longitudinal emittance, the so-called emittance exchange technique is commonly used; here, a dispersive beam is passed through a discrete or continuous absorber in such a way that high-energy particles traverse more material than low-energy particles. The net result is a reduction of the longitudinal emittance at the cost of simultaneously increasing the transverse emittance. By controlling the amount of emittance exchange, one can reduce the 6D emittance.

Muon colliders require a reduction of six orders of magnitude in the muon beam phase space, whereas neutrino factories benefit from the cooling. Various scenarios were recently put forward by the Muon Accelerator Staging Study (MASS) (127, 128), and for each of those scenarios there are corresponding cooling channel options based on vacuum RF or high-pressure gas-filled RF that can reach the desired design parameters.

**Figure 20** shows the evolution of the transverse and longitudinal normalized emittances in a cooling channel that uses vacuum RF (see Section 6.3.1). The beam comes out of the muon front

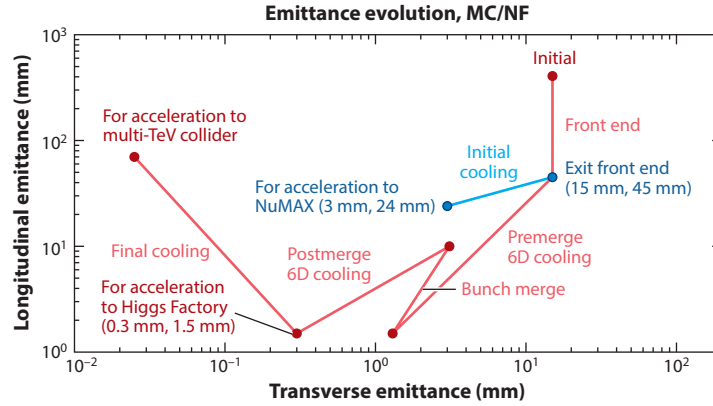


**Figure 20**

Emittance evolution for different applications. The blue line corresponds to the cooling needed for the NuMAX neutrino factory (NF) (127, 128), and the red line represents muon collider (MC) options. The cooling process starts in the top right corner. Abbreviation: 6D, six-dimensional.

end (after RF bunching) with a transverse normalized emittance of 15 mm (transverse beam size,  $\sigma_{\perp} = 8$  cm) and a longitudinal emittance of 45 mm (longitudinal beam size,  $\sigma_{\parallel} = 15$  cm). Twenty-one bunches selected by the front end are cooled in the premerge channel, followed by the bunch merge section combining all bunches into one. The resulting single bunch is then cooled further in the postmerge cooling channel, until the Higgs Factory muon collider design emittances of 0.3 mm transverse (beam size,  $\sigma_{\perp} = 2$  mm) and 1.5 mm longitudinal (beam size,  $\sigma_{\parallel} = 21$  mm) are reached. A multi-TeV collider will also require a final transverse cooling section (which increases the longitudinal emittance) in order to reach the design luminosity.

### 6.3. Six-Dimensional Cooling Channels

The front end of a muon facility (either a muon collider or a neutrino factory) has been optimized (129) to maximize the number muons collected ( $\mu^+$  and  $\mu^-$  are captured and transported simultaneously in a system of solenoids) in the momentum range from 10 to 300 MeV/c. It is in this momentum range that the initial stages of ionization cooling are most effective. It is also a regime where the number of muons captured per POT is quite high. For example, the current benchmark for the muon front end is  $\simeq 0.1 \mu^+$  in the momentum range from 100 to 300 MeV/c, per POT. In comparison, as stated in Section 3, nuSTORM collects  $\simeq 0.008 \mu^+$  in the  $\sim 0.8$  GeV/c momentum acceptance of the ring, per POT. In the following two sections, we provide an overview of two scenarios that can achieve the required 6D cooling necessary for the muon collider.

**6.3.1. Vacuum cooling channel.** In the vacuum cooling channel (VCC), each cell consists of solenoids for focusing that are tilted slightly to generate bending and dispersion, wedge-shaped absorbers where cooling takes place, and vacuum RF cavities to replenish the energy lost in the absorbers. The channel is tapered by changing the geometry of the lattice (magnetic field strength, RF frequency, absorber opening angle) progressively (130) to keep emittance away from the equilibrium, thereby improving cooling efficiency. **Figure 21a** shows the layout of one of the latter stages.

This scheme uses separate 6D ionization cooling channels for the two signs of the particle charge. In each, a channel first reduces the emittance of a train of muon bunches until they can

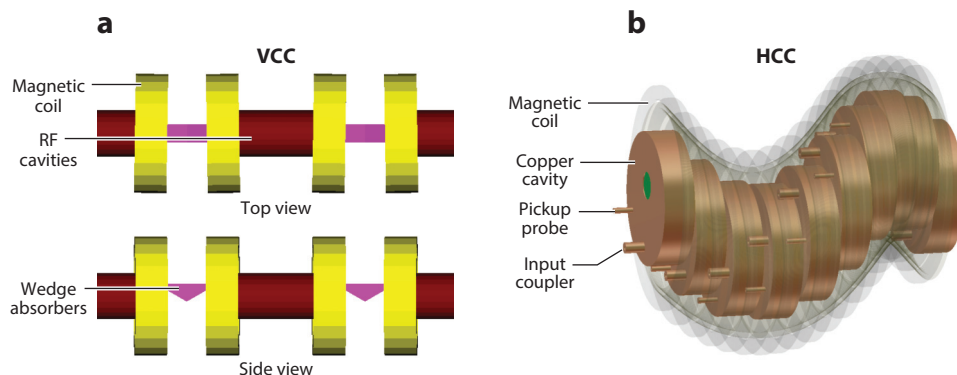


**Figure 21**

Six-dimensional cooling channels. (a) Schematics of one of the stages of the vacuum cooling channel (VCC). Yellow, magnetic coils for focusing and dispersion generation; red, radio-frequency (RF) cavities for replenishing the energy lost in the absorbers; magenta, solid LiH or liquid hydrogen, depending on the stage. (b) Conceptual design of the helical cooling channel (HCC). The RF cavities inside the magnetic coils are shown. The magnetic coils are semitransparent.

be injected into a bunch-merging system. The single muon bunches, one of each sign, are then sent through a second 6D cooling channel, where the transverse emittance is reduced as much as possible and the longitudinal emittance is cooled to a value below that needed for the collider. The beam can then be recombined and sent through a final cooling channel, using high-field solenoids, that cools the transverse emittance to the required value for a multi-TeV collider, while allowing the longitudinal emittance to grow.

The performance of the vacuum cooling channel was simulated using G4Beamline, and after a distance of 490 m (80 stages) the 6D emittance was reduced by a factor of 1,000 with a transmission of 40%. Decreasing the longitudinal emittance below 1.5 mm led to severe particle loss and emittance growth due to space-charge effects. Thus, after reaching this threshold, the beam was cooled in the transverse direction only. The simulated results are in agreement with theoretical predictions (131). Finally, a transverse emittance of 280  $\mu\text{m}$  can be achieved; this value is below the baseline requirement for a muon collider after the final 6D cooling sequence.

**6.3.2. High-pressure gas-filled cooling channel.** An alternative to the VCC is the homogeneous ionization absorber-filled helical cooling channel (HCC) (132–134). The primary magnetic components of the HCC are the solenoid and counteracting helical dipole to define the reference trajectory and the helical dipole gradient that controls the dispersion and provides transverse stability. **Figure 21b** shows the conceptual design of the helical cooling channel. High-pressure hydrogen gas-filled RF (HPRF) cavities are embedded inside the magnetic coils in the HCC. RF cavities are placed continuously along the helical beam path in the HCC magnet. High-pressure hydrogen in the cavity acts as a homogeneous ionization absorber. It also reduces the probability of electric breakdown in the RF cavity and allows higher operating  $E$  fields in strong magnetic fields. The breakdown suppression model has been experimentally verified, and no RF degradation due to the external magnetic field has been observed (135). The ultimate equilibrium emittances that can be reached are 0.6 mm in the transverse direction and 0.9 mm in the longitudinal direction, which could be translated into the desired values by using emittance exchange.

## 6.4. Six-Dimensional Cooling Tests

As mentioned above, muon ionization cooling improves the stored-muon flux at the neutrino factory and is absolutely crucial for a muon collider of any center-of-mass energy in order to achieve the required luminosity. The Muon Ionization Cooling Experiment (MICE; <http://mice.iit.edu/>) (136) will study four-dimensional ionization cooling, and research is under way to specify the scope of a follow-on 6D cooling experiment. MICE is referred to as a single-particle experiment; the four-momenta of single muons are measured before and after the cooling cell, and then input and output beam emittances are reconstructed from an ensemble of single-muon events. For 6D cooling, an experiment with a high-intensity pulsed muon beam is preferred. One feature of nuSTORM is that an appropriate low-energy muon beam with these characteristics can be provided in a straightforward fashion (see Section 3.2).

Thus, one of the key 6D cooling channel designs described in the previous sections can be tested at the nuSTORM facility without affecting the main neutrino physics programs. nuSTORM provides a low-energy muon source (**Figure 10**) with significant intensity ( $\sim 10^{10}$  muons per pulse in the 100–300 MeV/ $c$  momentum range). This beam can be produced simultaneously with the neutrino physics program at little additional cost. This is possible because nuSTORM requires an absorber to absorb pions remaining (approximately 50% of those injected into the ring) after the first straight section. Pions in the momentum range  $5 \text{ GeV}/c \pm 10\%$  are extracted to the absorber, along with many muons in the same momentum window (forward decays). The absorber will act as a degrader for these muons, producing the desired low-energy muon beam when an iron degrader of  $\sim 3.5 \text{ m}$  depth is used.

Once the bench test for the cooling channel is carried out with no beam, a section of the cooling channel long enough for appreciable 6D cooling can be used at the nuSTORM facility for a demonstration with beam. The corresponding study and simulation are under way.

## 7. MUON ACCELERATOR STAGING STUDY: RATIONALE FOR A STAGED APPROACH

The feasibility of the technologies required for muon colliders and neutrino factories must be validated before a facility based upon them can be proposed. Such validation is usually made in dedicated test facilities, which are specially designed to address the major issues. These test facilities are expensive to build and operate and are difficult to justify and fund, especially given that they are often useful only for technology development rather than for physics. An alternative approach, proposed by MASS, consists of a series of facilities built in stages, where each stage offers the following advantages:

1. Unique physics capabilities such that the facility obtains support and can be funded.
2. In parallel with the physics program, integration of an R&D platform using each stage as a source of particles to develop, test with beam, and validate a new technology that will be necessary for the following stages.
3. A system based on the new technology, which when validated to work could be used to improve the performance of an existing facility, even if it is not necessary for the present stage.
4. Operation of the new technology in a realistic environment, which is extremely useful not only to validate the new technology itself but also to acquire operational experience before using it in a subsequent stage.
5. Construction of each stage as an add-on to the previous stages, extensively reusing the equipment and systems already installed, such that the additional budget of each stage remains affordable.

The plan consists of a series of facilities with increasing complexity, each with performance characteristics providing unique physics reach:

1. nuSTORM. As described in this review, the facility provides both a powerful neutrino physics program and the infrastructure to test new technologies.
2. NuMAX. The initial LBL neutrino factory, optimized for a detector at Sanford Underground Research Facility (SURF) (137), affords a precise and well-characterized neutrino source that exceeds the capabilities of conventional superbeam technology.
3. NuMAX+. This full-intensity neutrino factory, upgraded from NuMAX, is the ultimate source to enable precision  $CP$ -violation measurements in the neutrino sector.
4. Higgs Factory. The baseline configurations of this collider are capable of providing between 3,500 (during startup operations) and 13,500 Higgs events per year ( $10^7$  s) with exquisite energy resolution.
5. Multi-TeV  $\mu^+\mu^-$  collider. If warranted by LHC results, a multi-TeV muon collider would likely offer the best performance and least cost for any lepton collider operating in the multi-TeV regime.

Each stage of this scheme can serve as a technology validation test bed for the subsequent stage. The key example is nuSTORM, which does not require any state-of-the-art R&D and at the same time can serve as a facility for a 6D cooling demonstration, as described in Section 6.4.

## 8. SUMMARY AND OUTLOOK

In this article, we have reviewed the potential of the nuSTORM facility. nuSTORM can simultaneously produce flavor-pure neutrino beams from the decays of both pions and muons and can also provide an intense low-energy muon beam at the same time from the same proton power. Thus, the nuSTORM facility can simultaneously (*a*) provide SBL oscillation measurements leading to a definitive solution to the question of sterile neutrinos and, should they exist, allow for the most comprehensive program to study their properties proposed to date; (*b*) make world-leading measurements of neutrino interactions that could be crucial to the success of planned LBL neutrino programs; and (*c*) host an excellent R&D platform for 6D muon ionization cooling channel bench and beam tests and, as such, act as a stepping stone toward future high-energy, high-intensity muon accelerator facilities.

The opportunities afforded by such a facility are great, but at present they lack the formal support required to become a reality. Because nuSTORM has a relatively short construction time and leads into a sustained R&D program, it has the potential to enhance the long-term prospects for neutrino physics, as well as sustain a nascent muon collider community. The growth and development of neutrino physics and energy-frontier science will require pursuing new ideas and making them viable. The anticipated long timescales of the next generation of facilities will eventually limit the growth of the field, if their pursuit completely precludes embracing new ideas and innovation.

## DISCLOSURE STATEMENT

The authors are not aware of any affiliations, memberships, funding, or financial holdings that might be perceived as affecting the objectivity of this review.

## ACKNOWLEDGMENTS

We thank our colleagues in the Muon Collider and Neutrino Factory communities in general and in particular our collaborators on nuSTORM, on MICE, and in MAP. We offer special thanks to

David Neuffer, who started down this path more than 30 years ago, and to Ao Liu, who has worked so tirelessly on developing the nuSTORM facility. The writing of this review was supported by the Fermi Research Alliance, LLC, under contract DE-AC02-07CH11359 with the US Department of Energy; the Muon Accelerator Program within the US Department of Energy; and the Science and Technology Facilities Council of the United Kingdom.

## LITERATURE CITED

1. Adey D, et al. arXiv:1308.6822 [physics.acc-ph] (2013)
2. Bross A. In *Proceedings of the 2013 North American Particle Accelerator Conference*, ed. T Satogata, C Petit-Jean-Genaz, VRW Schaa, pap. TUOBD4. JACoW.org: Jt. Accel. Conf. Website (2013)
3. Bross A. In *Proceedings of the 2013 European Physical Society Conference on High Energy Physics*, pap. EPS-HEP2013. Trieste, It.: Proc. Sci. (2013)
4. Geer S. *Phys. Rev. D* 57:6989 (1998)
5. Giesch M, Kuiper B, van der Meer S. *Nucl. Instrum. Methods* 20:58 (1963)
6. Choubey S, et al. arXiv:1112.2853 [hep-ex] (2011)
7. Abe K, et al. arXiv:1407.7389 [hep-ex] (2014)
8. Adams C, et al. arXiv:1307.7335 [hep-ex] (2013)
9. Agostino L. *J. Phys. Conf. Ser.* 566:012002 (2014)
10. Mohapatra R. *Phys. Rev. Lett.* 56:561 (1986)
11. Mohapatra R. *Phys. Rev. D* 34:3457 (1986)
12. Kusenko A, Takahashi F, Yanagida TT. *Phys. Lett. B* 693:144 (2010)
13. Abazajian K, et al. arXiv:1204.5379 [hep-ph] (2012)
14. Aguilar A, et al. *Phys. Rev. D* 64:112007 (2001)
15. Aguilar-Arevalo A, et al. *Phys. Rev. Lett.* 110:161801 (2013)
16. Anselmann P, et al. *Phys. Lett. B* 342:440 (1995)
17. Hampel W, et al. *Phys. Lett. B* 420:114 (1998)
18. Abdurashitov D, et al. *Phys. Rev. Lett.* 77:4708 (1996)
19. Abdurashitov J, et al. *Phys. Rev. C* 59:2246 (1999)
20. Abdurashitov J, et al. *Phys. Rev. C* 73:045805 (2006)
21. Mention G, et al. *Phys. Rev. D* 83:073006 (2011)
22. Mueller T, et al. *Phys. Rev. C* 83:054615 (2011)
23. Huber P. *Phys. Rev. C* 84:024617 (2011)
24. Huber P, Bross A, Palmer M. arXiv:1411.0629 [hep-ex] (2014)
25. Borodovsky L, et al. *Phys. Rev. Lett.* 68:274 (1992)
26. Armbruster B, et al. *Phys. Rev. D* 65:112001 (2002)
27. Astier P, et al. *Nucl. Phys. B* 611:3 (2001)
28. Antonello M, et al. arXiv:1209.0122 [hep-ex] (2012)
29. Ashie Y, et al. *Phys. Rev. D* 71:112005 (2005)
30. Cleveland B, et al. *Astrophys. J.* 496:505 (1998)
31. Kaether F, et al. *Phys. Lett. B* 685:47 (2010)
32. Abdurashitov J, et al. *Phys. Rev. C* 80:015807 (2009)
33. Hosaka J, et al. *Phys. Rev. D* 73:112001 (2006)
34. Aharmim B, et al. *Phys. Rev. C* 75:045502 (2007)
35. Aharmim B, et al. *Phys. Rev. C* 72:055502 (2005)
36. Aharmim B, et al. *Phys. Rev. Lett.* 101:111301 (2008)
37. Aharmim B, et al. arXiv:1109.0763 [nucl-ex] (2011)
38. Bellini G, et al. *Phys. Rev. Lett.* 107:141302 (2011)
39. Bellini G, et al. *Phys. Rev. D* 82:033006 (2010)
40. Aguilar-Arevalo AA, et al. *Phys. Rev. Lett.* 103:061802 (2009)
41. Cheng G, et al. *Phys. Rev. D* 86:052009 (2012)
42. Adamson P, et al. *Phys. Rev. D* 81:052004 (2010)

43. Adamson P, et al. *Phys. Rev. Lett.* 107:011802 (2011)
44. Declais Y, et al. *Nucl. Phys. B* 434:503 (1995)
45. Declais Y, et al. *Phys. Lett. B* 338:383 (1994)
46. Kuvshinnikov A, et al. *JETP Lett.* 54:253 (1991)
47. Vidyakin G, et al. *Sov. Phys. JETP* 66:243 (1987)
48. Kwon H, et al. *Phys. Rev. D* 24:1097 (1981)
49. Zacek G, et al. *Phys. Rev. D* 34:2621 (1986)
50. Apollonio M, et al. *Eur. Phys. J. C* 27:331 (2003)
51. Boehm F, et al. *Phys. Rev. D* 64:112001 (2001)
52. Abe Y, et al. *Phys. Rev. D* 86:052008 (2012)
53. Ahn J, et al. *Phys. Rev. Lett.* 108:191802 (2012)
54. Gando A, et al. *Phys. Rev. D* 83:052002 (2011)
55. Dydak F, et al. *Phys. Lett. B* 134:281 (1984)
56. Eitel K, et al. *Prog. Part. Nucl. Phys.* 48:89 (2002)
57. Auerbach L, et al. *Phys. Rev. C* 64:065501 (2001)
58. Kopp J, Maltoni M, Schwetz T. *Phys. Rev. Lett.* 107:091801 (2011)
59. Giunti C, Laveder M. *Phys. Lett. B* 706:200 (2011)
60. Karagiorgi G. arXiv:1110.3735 [hep-ph] (2011)
61. Giunti C, Laveder M. *Phys. Rev. D* 84:093006 (2011)
62. Giunti C, Laveder M. *Phys. Rev. D* 84:073008 (2011)
63. Giunti C, et al. *Phys. Rev. D* 86:113014 (2012)
64. Archidiacono M, et al. arXiv:1302.6720 [astro-ph.CO] (2013)
65. Kopp J, Machado P, Maltoni M, Schwetz T. arXiv:1303.3011 [hep-ph] (2013)
66. An F, et al. *Phys. Rev. Lett.* 113:141802 (2014)
67. Sousa A. arXiv:1502.07715 [hep-ex] (2015)
68. Abe K, et al. arXiv:1410.8811 [hep-ex] (2014)
69. Ade P, et al. *Astron. Astrophys.* 571:A16 (2014)
70. Hinshaw G, et al. arXiv:1212.5226 [astro-ph.CO] (2012)
71. Das S, et al. arXiv:1301.1037 [astro-ph.CO] (2013)
72. Reichardt C, et al. *Astrophys. J.* 755:70 (2012)
73. Story K, et al. arXiv:1210.7231 [astro-ph.CO] (2012)
74. Percival WJ, et al. *Mon. Not. R. Astron. Soc.* 401:2148 (2010)
75. Padmanabhan N, et al. arXiv:1202.0090 [astro-ph.CO] (2012)
76. Blake C, et al. *Mon. Not. R. Astron. Soc.* 418:1707 (2011)
77. Anderson L, et al. *Mon. Not. R. Astron. Soc.* 427:3435 (2013)
78. Hannestad S, Hansen RS, Tram T. *Phys. Rev. Lett.* 112:031802 (2014)
79. Dasgupta B, Kopp J. *Phys. Rev. Lett.* 112:031803 (2014)
80. Mirizzi A, Mangano G, Pisanti O, Saviano N. arXiv:1410.1385 [hep-ph] (2014)
81. Huber P, Mezzetto M, Schwetz T. *J. High Energy Phys.* 0803:021 (2008)
82. Neuffer DV. In *Proceedings of the Telemark Conference on Neutrino Mass*, ed. V Barger, D Cline, p. 199. New York: Am. Inst. Phys. (1980)
83. Neuffer DV, Liu A. In *Proceedings of the 4th International Particle Accelerator Conference*, ed. Z Dai, C Petit-Jean-Genaz, VRW Schaa, C Zhang, pap. TUPFI055. JACoW.org; Jt. Accel. Conf. Website (2013)
84. Liu A, Bross A, Neuffer D, Lee SY. In *Proceedings of the 2013 North American Particle Accelerator Conference*, ed. T Satogata, C Petit-Jean-Genaz, VRW Schaa, pap. TUPBA18. JACoW.org; Jt. Accel. Conf. Website (2013)
85. Lackowski T, et al. arXiv:1309.1389 [physics.ins-det] (2013)
86. Hylen J, et al. *Conceptual Design for the Technical Components of the Neutrino Beam for the Main Injector (NuMI)*. Batavia, IL: Fermi Natl. Accel. Lab. <http://inspirehep.net/record/448599/files/fermilab-tm-2018.PDF> (1997)
87. Wildner E. Presented at Int. Workshop Neutrino Fact. Future Neutrino Facil. (NUFACT14), Glasgow (2014)



88. Adey D, et al. arXiv:1305.1419 [physics.acc-ph] (2013)
89. Liu A, Bross A, Neuffer DV. In *Proceedings of the 5th International Particle Accelerator Conference*, ed. C Petit-Jean-Genaz, G Arduini, P Michel, VRW Schaa, pap. TUPRI005. JACoW.org: Jt. Accel. Conf. Website (2014)
90. Yamanoi Y, et al. *IEEE Trans. Magn.* 32:2147 (1996)
91. Roberts T. *G4beamline: a "Swiss Army Knife" for Geant4, optimized for simulating beamlines*. Version 2.12. <http://www.muonsinternal.com/muons3/G4beamline> (2013)
92. Liu A, Bross A, Neuffer DV. In *Proceedings of the 5th International Particle Accelerator Conference*, ed. C Petit-Jean-Genaz, G Arduini, P Michel, VRW Schaa, pap. IPAC-2014-TUPRI006. JACoW.org: Jt. Accel. Conf. Website (2014)
93. Neuffer DV. 2014. Presented at Int. Workshop Neutrino Fact. Future Neutrino Facil. (NUFACT14), Glasgow (2014)
- 93a. Liu A. *Design and simulation of the nuSTORM facility*. PhD thesis, Dep. Phys., Indiana Univ., Bloomington. <http://inspirehep.net/record/1370195/files/fermilab-thesis-2015-04.pdf> (2015)
94. Lagrange J. 2014. Presented at Int. Workshop Neutrino Fact. Future Neutrino Facil. (NUFACT14), Glasgow (2014)
95. Lagrange J, et al. In *Proceedings of the 5th International Particle Accelerator Conference*, ed. C Petit-Jean-Genaz, G Arduini, P Michel, VRW Schaa, pap. IPAC-2014-TUPRO073. JACoW.org: Jt. Accel. Conf. Website (2014)
96. Appleby R, et al. In *Proceedings of the 5th International Particle Accelerator Conference*, ed. C Petit-Jean-Genaz, G Arduini, P Michel, VRW Schaa, pap. IPAC-2014-TUPRI013. JACoW.org: Jt. Accel. Conf. Website (2014)
97. Soby L. *nuSTORM beam instrumentation*. eDMS doc. 1284677. Geneva: CERN. <https://edms.cern.ch/document/1284677/1/TAB3> (2013)
98. Guardincerri E. *J. Phys. Conf. Ser.* 404:012036 (2012)
99. Rubbia A. *J. Phys. Conf. Ser.* 408:012006 (2013)
100. Michael DG, et al. *Nucl. Instrum. Methods A* 596:190 (2008)
101. Ambrosio G, et al. *Design study for a staged very large hadron collider*. Fermilab-TM-2149. Batavia, IL: Fermi Natl. Accel. Lab. <http://ss.fnal.gov/archive/test-tm/2000/fermilab-tm-2149.pdf> (2001)
102. Vysotsky V, et al. *IEEE Trans. Appl. Supercond.* 20:402 (2010)
103. Foussart A, et al. *IEEE Trans. Appl. Supercond.* 22:42000505 (2012)
104. Wesche R, et al. In *Proceedings of the Workshop on Accelerator Magnet Superconductors, Design, and Optimization (WAMSDO)*, p. 68. Geneva: CERN. <http://cds.cern.ch/record/1163718/files/p68.pdf> (2009)
105. Adey D. 2014. Presented at Int. Workshop Neutrino Fact. Future Neutrino Facil. (NUFACT14), Glasgow (2014)
106. Mokhov N, Striganov S. *AIP Conf. Proc.* 896:50 (2007)
107. Andreopoulos C, et al. *Nucl. Instrum. Methods A* 614:87 (2010)
108. Apostolakis J, Wright DH. *AIP Conf. Proc.* 896:1 (2007)
109. Bayes R, et al. *Phys. Rev. D* 86:093015 (2012)
110. Hoecker A, et al. *Proc. Sci. ACAT*:040 (2007)
111. Brun R, Rademakers F. *Nucl. Instrum. Methods A* 389:81 (1997)
112. Huber P, Lindner M, Winter W. *Comput. Phys. Commun.* 167:195 (2005)
113. Baller B, et al. *J. Instrum.* 9:T05005 (2014)
114. de Gouvêa A, Kelly KJ, Kobach A. arXiv:1412.1479 [hep-ph] (2014)
115. Gallardo J, et al. *eConf C960625:R4* (1996)
116. Ankenbrandt CM, et al. *Phys. Rev. Spec. Top. Accel. Beams* 2:081001 (1999)
117. Alsharo'a MM, et al. *Phys. Rev. Spec. Top. Accel. Beams* 6:081001 (2003)
118. Parkhomchuk V, Skrinsky A. *Rev. Accel. Sci. Technol.* 1:237 (2008)
119. Neuffer D. *AIP Conf. Proc.* 156:201 (1987)
120. Geer S. *Annu. Rev. Nucl. Part. Sci.* 59:347 (2009)
121. Parkhomchuk V, Skrinsky A. *AIP Conf. Proc.* 352:7 (1996)
122. Neuffer DV. *Part. Accel.* 14:75 (1983)

123. Palmer R, et al. *Phys. Rev. Spec. Top. Accel. Beams* 8:061003 (2005)
124. Palmer M. In *Proceedings of the 5th International Particle Accelerator Conference*, ed. C Petit-Jean-Genaz, G Arduini, P Michel, VRW Schaa, pap. TUPME012. JACoW.org: Jt. Accel. Conf. Website (2014)
125. Palmer M. In *Proceedings of the 2013 International Workshop on Beam Cooling and Related Topics (COOL13)*, ed. LV Jørgenson, VRW Schaa, pap. MOAM2HA02. JACoW.org: Jt. Accel. Conf. Website (2013)
126. Torun Y, et al. In *Proceedings of the 1st International Particle Accelerator Conference*, ed. S Kurokawa, K Oide, pap. WEPE065. JACoW.org: Jt. Accel. Conf. Website (2010)
127. Delahaye JP, et al. arXiv:1308.0494 [physics.acc-ph] (2013)
128. Delahaye JP, et al. In *Proceedings of the 5th International Particle Accelerator Conference*, ed. C Petit-Jean-Genaz, G Arduini, P Michel, VRW Schaa, pap. IPAC-2014-WEZA02. JACoW.org: Jt. Accel. Conf. Website (2014)
129. Bogomilov M, et al. *Phys. Rev. Spec. Top. Accel. Beams* 17:121002 (2014)
130. Stratakis D, Fernow R, Berg J, Palmer R. *Phys. Rev. Spec. Top. Accel. Beams* 16:091001 (2013)
131. Stratakis D, Neuffer DV. In *Proceedings of the 5th International Particle Accelerator Conference*, ed. C Petit-Jean-Genaz, G Arduini, P Michel, VRW Schaa, pap. TUPME021. JACoW.org: Jt. Accel. Conf. Website (2014)
132. Derbenev Y, Johnson R. *Phys. Rev. Spec. Top. Accel. Beams* 8:041002 (2005)
133. Yonehara K. In *Proceedings of the 5th International Particle Accelerator Conference*, ed. C Petit-Jean-Genaz, G Arduini, P Michel, VRW Schaa, pap. TUPME014. JACoW.org: Jt. Accel. Conf. Website (2014)
134. Yonehara K. In *Proceedings of the 5th International Particle Accelerator Conference*, ed. C Petit-Jean-Genaz, G Arduini, P Michel, VRW Schaa, pap. TUPME015. JACoW.org: Jt. Accel. Conf. Website (2014)
135. Hanlet P, et al. In *Proceedings of the 2006 European Particle Accelerator Conference*, ed. C Prior, no. TUPCH147. Mulhouse, Fr.: Eur. Phys. Sci. Accel. Group (2006)
136. Kaplan D, Snopok P, Dobbs A. In *Proceedings of the 5th International Particle Accelerator Conference*, ed. C Petit-Jean-Genaz, G Arduini, P Michel, VRW Schaa, pap. THPRI030. JACoW.org: Jt. Accel. Conf. Website (2014)
137. Heise J. *AIP Conf. Proc.* 1604:331 (2014)